Finite element based model order reduction for parametrized one-way coupled steady state linear thermo-mechanical problems

Nirav Vasant Shah[a], Michele Girfoglio[a], Peregrina Quintela[b,c], Gianluigi Rozza[a,*], Alejandro Lengomin[d], Francesco Ballarin[e], Patricia Barral[b,c]

[a]*Scuola Internazionale Superiore di Studi Avanzati (SISSA), via Bonomea 265, Trieste, 34136, Italy*
[b]*Instituto Tecnolóxico de Matemática Industrial (ITMATI), currently integrated in CITMAGA, s/n, Campus Vida, Rúa de Constantino Candeira, Santiago de Compostela, 15705, Spain*
[c]*Departamento de Matemática Aplicada, Universidade de Santiago de Compostela, Santiago de Compostela, 15782, Spain*
[d]*Primary & By-Products Department, ArcelorMittal, Global R&D Asturias, P.O. Box 90, Avilés, 33400, Spain*
[e]*Department of Mathematics and Physics, Catholic University of the Sacred Heart, via Musei 41, Brescia, 25121, Italy*

Abstract

This contribution focuses on the development of Model Order Reduction (MOR) for one-way coupled steady state linear thermo-mechanical problems in a finite element setting. We apply Proper Orthogonal Decomposition (POD) for the computation of reduced basis space. On the other hand, for the evaluation of the modal coefficients, we use two different methodologies: the one based on the Galerkin projection (G) and the other one based on Artificial Neural Network (ANN). We aim to compare POD-G and POD-ANN in terms of relevant features including errors and computational efficiency. In this context, both physical and geometrical parametrization are considered. We also carry out a validation of the Full Order Model (FOM) based on customized benchmarks in order to provide a complete computational pipeline. The framework proposed is applied to a relevant industrial problem related to the investigation of thermo-mechanical phenomena arising in blast furnace hearth walls.

Keywords: Thermo-mechanical problems, Finite element method, Geometric and physical parametrization, Proper orthogonal decomposition, Galerkin projection, Artificial neural network, Blast furnace.

1. Introduction

Due to technological developments occurred in recent years, the high-fidelity numerical computations, based on the so-called Full Order Models (FOM) (e.g., finite element or finite volume methods), are required to be performed for many configurations. This puts the computational resources under considerable stress. In this context, Model Order Reduction (MOR) has been introduced as an efficient tool to accelerate the computations with "affordable" and "controllable" loss of accuracy. The faster computations obtained by MOR helped in many query contexts, e.g. quick transfer of computational results to industrial problems.

The basic idea on which MOR is based is related to the fact that often the parametric dependence of the problem at hand has an intrinsic dimension much lower than the number of degrees of freedom associated to the governing FOM. The development of a MOR consists in two main steps. The first one is the so-called *offline* stage when a database of several high-fidelity solutions is collected by solving the FOM for different values of physical and/or geometrical parameters. Then all the solutions are combined and compressed to extract a set of basis functions that approximate the low-dimensional manifold on which the solution lies. The second step is the *online* stage when the information obtained in the *offline* stage is used to efficiently compute the solutions for new parameters instances. For a comprehensive review on MOR, the reader is referred to, e.g., [3, 8, 10, 11, 24, 28, 43, 50].

In this work, we address the development of a MOR framework in a Finite Element (FE) environment for one-way coupled steady state linear thermo-mechanical problems. In the literature different MOR techniques have been proposed

---

*Corresponding author
Email addresses: shah.nirav@sissa.it (Nirav Vasant Shah), michele.girfoglio@sissa.it (Michele Girfoglio), peregrina.quintela@usc.es (Peregrina Quintela), gianluigi.rozza@sissa.it (Gianluigi Rozza), alejandro.lengomin@arcelormittal.com (Alejandro Lengomin), francesco.ballarin@unicatt.it (Francesco Ballarin), patricia.barral@usc.es (Patricia Barral)

in the context of thermo-mechanical problems. Guérin et al. [23] developed Rational Craig-Hale methodology for the investigation of thermo-mechanical coupling effects in turbomachinery. Benner et al. [9] compared the performance of Proper Orthogonal Decomposition (POD), Balanced Truncation, Padé approach and iterative rational Krylov algorithm for the approximation of the transient thermal field concerning an optimal sensor placement problem for a thermo-elastic solid body model. Zhang et al. [60] introduced reduced order variational multiscale enrichment method and tested their approach on proper benchmark tests related to the thermo-mechanical loading applied to a 2D composite beam and a functionally graded composite beam. More recently, Hernández-Beccero et al. [26] used Krylov Modal Subspace method for thermo-mechanical models as applicable to machine tools. We highlight that all these works are focused on MOR for the efficient reconstruction of the time evolution of the thermo-mechanical field. Regarding steady state problems, such as those dealt with in this work, Hoang et al. [31] used a two-field reduced basis algorithm based on the greedy algorithm in a physical parametrization setting. However, here we consider not only physical parameters but also geometrical ones. Concerning the methodology adopted, we use POD for the construction of reduced basis space. On the other hand, for the computation of the reduced coefficients, we consider two different approaches: a standard Galerkin projection (G) and Artificial Neural Network (ANN). POD-G aims to generate a MOR by a projection of the governing equations onto the POD space. So, the reduced coefficients associated to the POD bases are obtained by solving a set of algebraic equations. On the other hand, POD-ANN belongs to the category of machine learning methods based on systems that learn from data. In this framework, the reduced coefficients are computed by the employment of a properly trained neural network. There is a broad range of strategies for the development of new deep learning architectures for non-intrusive MOR approaches, i.e. without the need to access to FOM implementation: see, e.g., [27, 49, 56, 16, 41, 18, 58, 2, 17, 38]. We compare POD-G and POD-ANN in terms of relevant computational features including errors and speed up. From this viewpoint, the present contribution draws inspiration by [27] in which it has been shown that POD-ANN performs better than POD-G both in terms of efficiency and accuracy for steady state problems in heat transfer and fluid dynamics. We underline that whilst in [27] nonlinear problems are addressed, here we deal with a linear modeling framework by obtaining significantly different results. Our approach is applied within an industrial framework related to the investigation of thermo-mechanical phenomena arising in blast furnace hearth walls. Neural networks can in theory represent any functional relationship between inputs and output. However, many applications are still unexplored, and we retain that the use of POD-ANN method in the context of thermo-mechanical problems of industrial interest could open the door towards the application of deep learning techniques to new multiphysics scenarios.

The workflow of this paper is organized as follows. In Sec. 2 the physical problem related to the blast furnace hearth walls is introduced. The full order model in strong formulation is described in Sec. 3. The corresponding weak formulation is then derived in Sec. 4 and the finite element analysis is introduced in Sec. 5. Subsequently, in Sec. 6, the MOR approach is described, and results obtained are shown and discussed. Conclusions and perspectives are drawn in Sec. 7. Finally, we dedicate a wide Appendix to the FOM validation in order to show the functionality of the developed finite element code.

2. Physical problem

Steelmaking is a very old process that has contributed to the development of technological societies since ancient times. The previous stage is the ironmaking process, which is performed inside a blast furnace, whose general layout is shown in Figure 1. It is a metallurgical reactor used to produce hot metal from iron ore. For further details the reader is referred, e.g., to [15, 20].

The blast furnace operates at a high temperature (up to 1500 °C). The associated thermal stresses significantly limit the overall blast furnace campaign period. In this context, thermo-mechanical modeling has been used extensively either to support experimental campaign or to design various components. Vázquez-Fernández et al. [57] simulated the stationary heat transfer in a trough of a blast furnace to ensure durability based on the location of critical isotherm. In Barral et al [5, 6], the transient behaviour of the temperature during a tapping and a full campaign cycle was analyzed. Numerical modeling of heat flows in the blast furnace hearth lining was used by Swartling M. et al. [55] for improving experimental assessment. Thermo-mechanical modeling of blast furnace hearth was also developed by Brulin et al. [14]: they used micro-macro approach with homogenization method for replacing bricks and mortars by an equivalent material.

The blast furnace operates under different conditions, each of which is governed by a different mathematical model. Considering the objectives of the present work, the following simplifications are considered:
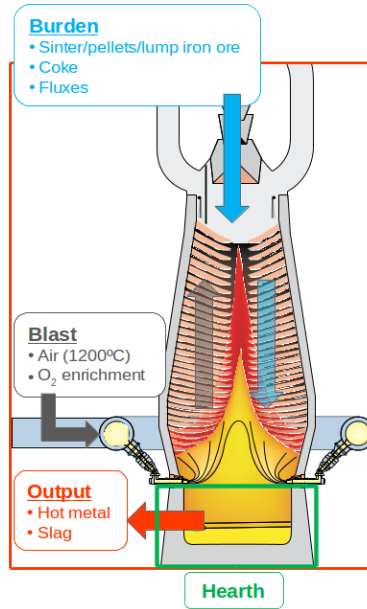
Figure 1: Blast furnace [Courtesy: ArcelorMittal, Spain].

- Taphole operation is not part of this study. The perforation action of the taphole and the important pressures in the draining of the hot metal and slag produce important mechanical stresses located in the area that requires a deeper analysis and that is out of the scope of this work.

- Since the objective is to be able to calculate in real time the effects of wall design on blast furnace operation, we focus on the steady state operations.

- We assume that the hearth is made up of a single homogeneous, elastic, and isotropic material with temperature-independent material properties.

- Heat transfer only by conduction within hearth walls will be considered. The temperature of the molten metal inside the hearth is assumed constant and known. Therefore, the fluid region will not be part of the problem.

3. Full order model

In this section, we discuss the mathematical formulation corresponding to the physical problem described in Sec. 2. We present the thermo-mechanical model in cylindrical coordinates endowed with suitable boundary conditions in Sec. 3.1. Then, we introduce the axisymmetric hypothesis and derive the axisymmetric thermo-mechanical model in Sec. 3.2.
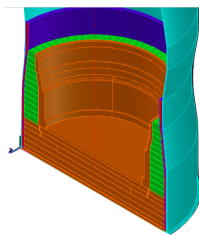
(a) Section of hearth geometry [Courtesy : ArcelorMittal].
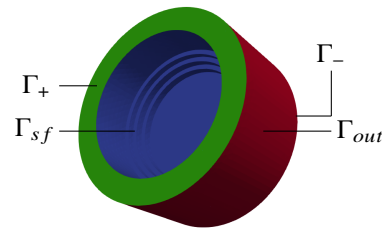
(b) Simplified domain Ω and its boundaries.

Figure 2: Hearth geometry: three dimensional domains, the real one (a) and its simplification as well as its boundaries (b).
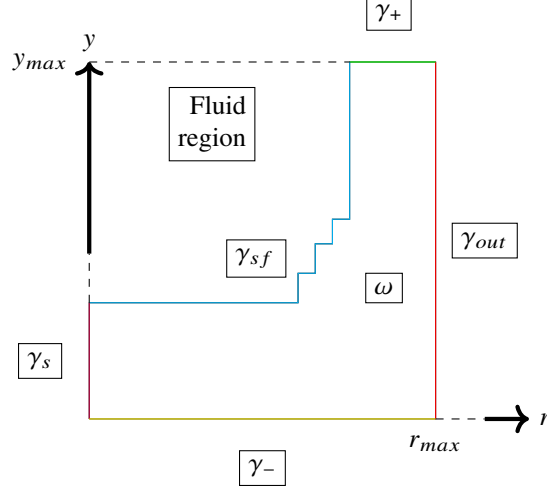
3

Figure 3: Vertical section of the hearth geometry ω and its boundaries.

3.1. Thermo-mechanical model in cylindrical coordinates

We consider the three dimensional domain Ω as in Figure 2 (b), corresponding to the simplified hearth geometry. We represent the displacement vector field as $\vec{u}$ and the temperature scalar field as T. Based on the simplifications listed in Sec. 2, the energy and momentum conservation equations [12, 21, 22] can be written in a cylindrical coordinates system, (r, y, θ), with $(r, y) \in \omega$, the vertical cross section of Ω in $r - y$ plane, (see Figure 3), and $\theta \in [0, 2\pi)$, as,

$$-\frac{1}{r}\frac{\partial}{\partial r}\left(rk\frac{\partial T}{\partial r}\right) - \frac{\partial}{\partial y}\left(k\frac{\partial T}{\partial y}\right) - \frac{1}{r}\frac{\partial}{\partial \theta}\left(\frac{k}{r}\frac{\partial T}{\partial \theta}\right) = Q \,, \text{ in } \Omega \,, \tag{1}$$

$$\frac{\partial \sigma_{rr}}{\partial r} + \frac{\partial \sigma_{ry}}{\partial y} + \frac{1}{r}\frac{\partial \sigma_{r\theta}}{\partial \theta} + \frac{\sigma_{rr} - \sigma_{\theta\theta}}{r} + f_{0,r} = 0 \,, \text{ in } \Omega \,,$$

$$\frac{\partial \sigma_{r\theta}}{\partial r} + \frac{\partial \sigma_{\theta y}}{\partial y} + \frac{1}{r}\frac{\partial \sigma_{\theta\theta}}{\partial \theta} + 2\frac{\sigma_{r\theta}}{r} + f_{0,\theta} = 0 \,, \text{ in } \Omega \,, \tag{2}$$

$$\frac{\partial \sigma_{ry}}{\partial r} + \frac{1}{r}\frac{\partial \sigma_{\theta y}}{\partial \theta} + \frac{\partial \sigma_{yy}}{\partial y} + \frac{\sigma_{ry}}{r} + f_{0,y} = 0 \,, \text{ in } \Omega \,.$$

Here $\vec{f}_0$ is the body force density term, Q is the heat source term and $k > 0$ is the thermal conductivity tensor. The thermo-mechanical stress tensor σ is related to the strain tensor ε through the Hooke's law:

$$\sigma(\vec{u})[T] = \lambda \,\text{Tr}(\varepsilon(\vec{u}))I + 2\mu\varepsilon(\vec{u}) - (2\mu + 3\lambda)\alpha(T - T_0)I \,, \tag{3}$$

where T_0 is the reference temperature, ε is defined as,

$$\varepsilon(\vec{u}) = \frac{1}{2}(\nabla\vec{u} + \nabla\vec{u}^T) \,, \tag{4}$$

α is the thermal expansion coefficient, and λ and μ are the Lamé parameters of the material. These latter can be expressed in terms of Young modulus, E, and Poisson ratio, ν, as:

$$\mu = \frac{E}{2(1 + \nu)} \,, \quad \lambda = \frac{E\nu}{(1 - 2\nu)(1 + \nu)} \,. \tag{5}$$

If A denotes the matrix,

$$A = \frac{E}{(1 - 2\nu)(1 + \nu)}\begin{bmatrix} 1 - \nu & \nu & \nu & 0 & 0 & 0 \\ \nu & 1 - \nu & \nu & 0 & 0 & 0 \\ \nu & \nu & 1 - \nu & 0 & 0 & 0 \\ 0 & 0 & 0 & \frac{1-2\nu}{2} & 0 & 0 \\ 0 & 0 & 0 & 0 & \frac{1-2\nu}{2} & 0 \\ 0 & 0 & 0 & 0 & 0 & \frac{1-2\nu}{2} \end{bmatrix} \,, \tag{6}$$

4

the stress-strain relationship (3) can be expressed in vector formulation as,

$$\{\boldsymbol{\sigma}(\overrightarrow{u})[T]\} = \boldsymbol{A}\{\boldsymbol{\varepsilon}(\overrightarrow{u})\} - (2\mu + 3\lambda)\alpha(T - T_0)\{\boldsymbol{I}\} , \tag{7}$$

where the following column vectors have been considered:

$$\{\boldsymbol{\sigma}\} = \{\sigma_{rr} \quad \sigma_{yy} \quad \sigma_{\theta\theta} \quad \sigma_{y\theta} \quad \sigma_{r\theta} \quad \sigma_{ry}\}^T ,$$
$$\{\boldsymbol{\varepsilon}\} = \{\varepsilon_{rr} \quad \varepsilon_{yy} \quad \varepsilon_{\theta\theta} \quad 2\varepsilon_{y\theta} \quad 2\varepsilon_{r\theta} \quad 2\varepsilon_{ry}\}^T , \tag{8}$$
$$\{\boldsymbol{I}\} = \{1 \quad 1 \quad 1 \quad 0 \quad 0 \quad 0\}^T .$$

We introduce the notations for the boundaries of the domain Ω (Figure 2), and its vertical cross section in $r - y$ plane, ω (Figure 3):

$$\Gamma_{out} = \partial\Omega \cap (r \equiv r_{max}) = \gamma_{out} \times [0, 2\pi) ,$$
$$\Gamma_+ = \partial\Omega \cap (y \equiv y_{max}) = \gamma_+ \times [0, 2\pi) ,$$
$$\Gamma_- = \partial\Omega \cap (y \equiv 0) = \gamma_- \times [0, 2\pi) , \tag{9}$$
$$\Gamma_{sf} = \partial\Omega \backslash (\Gamma_{out} \cup \Gamma_+ \cup \Gamma_-) = \gamma_{sf} \times [0, 2\pi) ,$$
$$\gamma_s = \partial\omega \cap (r \equiv 0) ,$$

where $r_{max} \in \mathbb{R}^+$ and $y_{max} \in \mathbb{R}^+$.

Moreover, on the boundary, we define normal force σ_n and tangential force $\overrightarrow{\sigma_t}$ as follows:

$$\sigma_n = (\boldsymbol{\sigma}\overrightarrow{n}) \cdot \overrightarrow{n} , \quad \overrightarrow{\sigma_t} = \boldsymbol{\sigma}\overrightarrow{n} - \sigma_n\overrightarrow{n} , \tag{10}$$

where $\overrightarrow{n}$ is the unit normal vector that is directed outwards from Ω.

- On the upper boundary, Γ_+, the applied force, $\overrightarrow{g}_+$, and the density of heat flux, q_+, are known. Therefore, the following boundary conditions are considered:

$$(-k\nabla T) \cdot \overrightarrow{n} = q_+ , \quad \boldsymbol{\sigma}\overrightarrow{n} = \overrightarrow{g}_+ . \tag{11}$$

- On the bottom boundary, Γ_-, the convection heat transfer occurs with the heat exchanger at temperature T_- and heat transfer coefficient $h_{c,-}$. The normal displacement is null, and we denote with $\overrightarrow{g}_-$ the shear force. Therefore, it is verified:

$$(-k\nabla T) \cdot \overrightarrow{n} = h_{c,-}(T - T_-) , \quad \overrightarrow{u} \cdot \overrightarrow{n} = 0 , \quad \overrightarrow{\sigma_t} = \overrightarrow{g}_- . \tag{12}$$

- On the inner boundary, Γ_{sf}, convection heat transfer with the fluid phase occurs and hydrostatic pressure g_{sf} is acting. So, the following boundary conditions are considered:

$$(-k\nabla T) \cdot \overrightarrow{n} = h_{c,f}(T - T_f) , \quad \boldsymbol{\sigma}\overrightarrow{n} = \overrightarrow{g}_{sf} , \tag{13}$$

where T_f is the fluid temperature, assumed to be known and constant at the steady state, and $h_{c,f}$ is the convective heat transfer coefficient. In addition, $\overrightarrow{g}_{sf} = -g_{sf}\overrightarrow{n}$.

- On the outer boundary, Γ_{out}, a convective heat flux and known applied force $\overrightarrow{g}_{out}$ are assumed:

$$(-k\nabla T) \cdot \overrightarrow{n} = h_{c,out}(T - T_{out}) , \quad \boldsymbol{\sigma}\overrightarrow{n} = \overrightarrow{g}_{out} , \tag{14}$$

$h_{c,out}$ being the convective heat transfer coefficient and T_{out} the ambient temperature.

3.2. Axisymmetric thermo-mechanical model

In the context of blast furnace application, the body force density term $\overrightarrow{f_0}$, as well as surface forces, $\overrightarrow{g}_+, \overrightarrow{g}_-, \overrightarrow{g}_{sf}$, $\overrightarrow{g}_{out}$, have zero component in $\overrightarrow{e_\theta}$ direction and they do not depend on θ. Besides, the heat source term, Q, the heat flux density, q_+, the heat transfer coefficients, $h_{c,-}, h_{c,f}, h_{c,out}$, and temperatures T_-, T_f, T_{out} are assumed to be only dependent on (r, y) coordinates. Therefore, a symmetry hypothesis is applicable that leads to significant computational savings.

The associated axisymmetric model is reduced to consider conservation equations (1), (2) defined in ω and the boundary conditions (11) - (14), where the Γ boundaries are replaced by γ such that $\Gamma = (\gamma \backslash \gamma_s) \times [0, 2\pi)$ (see Figures 2 and 3, and definitions (9)). Moreover, the usual symmetry conditions on γ_s are added:

$$(-k\nabla T) \cdot \overrightarrow{n} = 0 \ , \ \overrightarrow{u} \cdot \overrightarrow{n} = 0 \ , \ \overrightarrow{\sigma_t} = \overrightarrow{0} \ . \tag{15}$$

Therefore, the axisymmetric thermo-mechanical model can be summarized as:

- **Thermal model**:

$$-\frac{1}{r}\frac{\partial}{\partial r}\left(rk\frac{\partial T}{\partial r}\right) - \frac{\partial}{\partial y}\left(k\frac{\partial T}{\partial y}\right) = Q \ , \ \text{in } \omega \ , \tag{16}$$

  with boundary conditions:

$$
\begin{aligned}
\text{on } \gamma_+ \ &: \ -k\frac{\partial T}{\partial y} = q_+ \ , \\
\text{on } \gamma_- \ &: \ k\frac{\partial T}{\partial y} = h_{c,-}(T - T_-) \ , \\
\text{on } \gamma_{sf} \ &: \ -k\frac{\partial T}{\partial r}n_r - k\frac{\partial T}{\partial y}n_y = h_{c,f}(T - T_f) \ , \\
\text{on } \gamma_{out} \ &: \ -k\frac{\partial T}{\partial r} = h_{c,out}(T - T_{out}) \ , \\
\text{on } \gamma_s \ &: \ \frac{\partial T}{\partial r} = 0 \ .
\end{aligned}
\tag{17}
$$

- **Mechanical model**:

$$
\begin{aligned}
\frac{\partial \sigma_{rr}}{\partial r} + \frac{\partial \sigma_{ry}}{\partial y} + \frac{\sigma_{rr} - \sigma_{\theta\theta}}{r} + f_{0,r} = 0 \ , \ \text{in } \omega \ , \\
\frac{\partial \sigma_{ry}}{\partial r} + \frac{\partial \sigma_{yy}}{\partial y} + \frac{\sigma_{ry}}{r} + f_{0,y} = 0 \ , \ \text{in } \omega \ ,
\end{aligned}
\tag{18}
$$

In vector notation, axisymmetric stress-strain relationship can be expressed as,

$$\{\boldsymbol{\sigma}(\overrightarrow{u})[T]\} = \boldsymbol{A}\{\boldsymbol{\varepsilon}(\overrightarrow{u})\} - (2\mu + 3\lambda)\alpha(T - T_0)\{\boldsymbol{I}\} \ ,$$

$$
\boldsymbol{A} = \frac{E}{(1-2\nu)(1+\nu)}\begin{bmatrix} 1-\nu & \nu & \nu & 0 \\ \nu & 1-\nu & \nu & 0 \\ \nu & \nu & 1-\nu & 0 \\ 0 & 0 & 0 & \frac{1-2\nu}{2} \end{bmatrix} \ ,
$$

$$\{\boldsymbol{\sigma}\} = \{\sigma_{rr} \quad \sigma_{yy} \quad \sigma_{\theta\theta} \quad \sigma_{ry}\}^T \ ,$$

$$\{\boldsymbol{\varepsilon}\} = \{\varepsilon_{rr} \quad \varepsilon_{yy} \quad \varepsilon_{\theta\theta} \quad 2\varepsilon_{ry}\}^T \ ,$$

$$\{\boldsymbol{I}\} = \{1 \quad 1 \quad 1 \quad 0\}^T \ ,$$

$$\tag{19}$$

with the boundary conditions :

$$
\begin{aligned}
\text{on } \gamma_+ &: \sigma_{ry} = g_{+,r}, \ \sigma_{yy} = g_{+,y}, \\
\text{on } \gamma_- &: u_y = 0, \ \sigma_{ry} = -g_{-,r}, \\
\text{on } \gamma_{sf} &: \sigma_{rr} n_r + \sigma_{ry} n_y = g_{sf,r}, \\
&\quad\ \sigma_{ry} n_r + \sigma_{yy} n_y = g_{sf,y}, \\
\text{on } \gamma_{out} &: \sigma_{rr} = g_{out,r}, \ \sigma_{ry} = g_{out,y}, \\
\text{on } \gamma_s &: u_r = 0, \ \sigma_{ry} = 0.
\end{aligned}
\tag{20}
$$

4. Weak formulation of axisymmetric thermo-mechanical model

In this section, we derive the weak formulation related to the axisymmetric thermo-mechanical model (16)-(20). First, in Sec. 4.1, we introduce the relevant function spaces for temperature and displacement fields as well as for the model data, including boundary conditions, physical properties, and source terms, such that the problem is well defined. Next, the weak formulations for the thermal and mechanical problems are reported in Sec. 4.2 and 4.3, respectively.

4.1. Functional spaces

For data of both thermal and mechanical problem, we introduce the weighted Sobolev spaces, $L_r^2(\omega)$, with norm $|| \cdot ||_{L_r^2(\omega)}$ as,

$$
L_r^2(\omega) = \left\{ f : \omega \mapsto \mathbb{R}, \ \int_\omega f^2 r dr dy < \infty \right\},
$$

$$
||f||_{L_r^2(\omega)}^2 = \int_\omega f^2 r dr dy.
\tag{21}
$$

Analogously, given γ a subset of $\partial\omega$, the boundary of ω,

$$
L_r^2(\gamma) = \left\{ g : \gamma \mapsto \mathbb{R}, \int_\gamma g^2 r d\gamma < \infty \right\}.
\tag{22}
$$

Let $L^\infty(\omega)$ be the space

$$
L^\infty(\omega) = \{ f : \omega \mapsto \mathbb{R}, \sup_\omega |f| \leq C, \ C \geq 0 \},
$$

$$
||f||_{L^\infty(\omega)} = \sup_\omega |f|.
\tag{23}
$$

Analogously, $L^\infty(\gamma)$ is defined.

For the temperature, we introduce the weighted Sobolev space, $H_r^1(\omega)$, with norm $|| \cdot ||_{H_r^1(\omega)}$ as,

$$
H_r^1(\omega) = \left\{ \psi : \omega \mapsto \mathbb{R}, \ \int_\omega \left(\psi^2 + \left(\frac{\partial \psi}{\partial r} \right)^2 + \left(\frac{\partial \psi}{\partial y} \right)^2 \right) r dr dy < \infty \right\},
$$

$$
||\psi||_{H_r^1(\omega)}^2 = \int_\omega \left(\psi^2 + \left(\frac{\partial \psi}{\partial r} \right)^2 + \left(\frac{\partial \psi}{\partial y} \right)^2 \right) r dr dy.
\tag{24}
$$

On the other hand, the following space $\mathbb{V}$ for the displacement is considered:

$$
\mathbb{V} = (H_r^1(\omega) \cap L_{1/r}^2(\omega)) \times H_r^1(\omega).
\tag{25}
$$

It will be equipped with the inner product,

$$
< \vec{u}, \vec{\phi} >_{\mathbb{V}} = \int_\omega \left(\phi_r u_r + \phi_y u_y + \frac{\partial u_r}{\partial r} \frac{\partial \phi_r}{\partial r} + \frac{\partial u_r}{\partial y} \frac{\partial \phi_r}{\partial y} + \frac{u_r}{r} \frac{\phi_r}{r} + \frac{\partial u_y}{\partial r} \frac{\partial \phi_y}{\partial r} + \frac{\partial u_y}{\partial y} \frac{\partial \phi_y}{\partial y} + \frac{\partial u_r}{\partial y} \frac{\partial \phi_y}{\partial r} + \frac{\partial u_y}{\partial r} \frac{\partial \phi_r}{\partial y} \right) r dr dy,
$$

$$
\tag{26}
$$

and with the norm,

$$||\overrightarrow{\phi}||_{\mathbb{V}}^2 = <\overrightarrow{\phi}, \overrightarrow{\phi}>_{\mathbb{V}} \ . \tag{27}$$

Its closed and convex subspace $\mathbb{U}$,

$$\mathbb{U} = \{\overrightarrow{\phi} = (\phi_r \ \phi_y) \in \mathbb{V}, \ \phi_y = 0 \text{ on } \gamma_-, \ \phi_r = 0 \text{ on } \gamma_s \} \ , \tag{28}$$

will be the set of admissible displacements. The subspace $\mathbb{U}$ is equipped with the same norm as spave $\mathbb{V}$ i.e. $||\overrightarrow{\phi}||_{\mathbb{U}} = ||\overrightarrow{\phi}||_{\mathbb{V}}, \forall \overrightarrow{\phi} \in \mathbb{U}$.

Finally, the function space for stress tensor is defined as,

$$\mathbb{S} = \{\boldsymbol{\sigma} = [\sigma_{ij}] \in [L_r^2(\omega)]^{3\times3}, \sigma_{ij} = \sigma_{ji}, \sigma_{\alpha3} = 0, \alpha = 1, 2\} \ . \tag{29}$$

For more details the reader is referred, e.g., to [29, 30, 35].

4.2. Weak formulation for thermal model

We assume the following hypotheses on the data:

(TH1) The heat source term, Q, is such that
$$Q \in L_r^2(\omega) \ .$$

(TH2) The convection temperatures, T_{sf}, T_- and T_{out}, as well as the boundary heat flux q_+ are such that

$$T_{sf} \in L_r^2(\gamma_{sf}), \ T_- \in L_r^2(\gamma_-), \ T_{out} \in L_r^2(\gamma_{out}), \ q_+ \in L_r^2(\gamma_+) \ .$$

(TH3) The thermal conductivity $k(r, y)$ and the convective heat transfer coefficients, $h_{c,f}(r, y)$, $h_{c,out}(r, y)$ and $h_{c,-}(r, y)$ are such that

$$k(r, y) \in L^\infty(\omega), \ k(r, y) > k_0 > 0 \ ,$$
$$h_{c,f}(r, y) \in L^\infty(\gamma_{sf}), \ h_{c,f}(r, y) > h_{c,f,0} > 0 \ ,$$
$$h_{c,out}(r, y) \in L^\infty(\gamma_{out}), \ h_{c,out}(r, y) > h_{c,out,0} > 0 \ ,$$
$$h_{c,-}(r, y) \in L^\infty(\gamma_-), \ h_{c,-}(r, y) > h_{c,-,0} > 0 \ ,$$

where k_0, $h_{c,f,0}$, $h_{c,out,0}$ and $h_{c,-,0}$ are suitable constants.

In order to propose a weak formulation for the thermal model (16) - (17), in the following we assume sufficient regularity to perform the calculations. We multiply the energy equation (16) by $r\psi(r, y)$, integrate over the domain ω with respect to (r, y) variables, apply Gauss divergence theorem and use boundary conditions (17) to obtain:

$$\int_\omega rk \left(\frac{\partial T}{\partial y} \frac{\partial \psi}{\partial y} + \frac{\partial T}{\partial r} \frac{\partial \psi}{\partial r} \right) drdy + \int_{\gamma_{sf}} \psi h_{c,f} Tr d\gamma + \int_{\gamma_{out}} \psi h_{c,out} Tr d\gamma +$$
$$\int_{\gamma_-} \psi h_{c,-} Tr d\gamma = \int_\omega \psi Q r drdy + \int_{\gamma_{sf}} \psi h_{c,f} T_f r d\gamma + \tag{30}$$
$$\int_{\gamma_{out}} \psi h_{c,out} T_{out} r d\gamma + \int_{\gamma_-} \psi h_{c,-} T_- r d\gamma - \int_{\gamma_+} \psi q^+ r d\gamma \ .$$

It is to be noted that under assumptions (TH1)-(TH3) all integrals of the proposed weak formulation are well defined for all $T, \psi \in H_r^1(\omega)$. The left hand side of equation (30) is bilinear and symmetric. So, we define in $H_r^1(\omega) \times H_r^1(\omega)$ the operator:

$$a_T(T, \psi) = \int_\omega rk \left(\frac{\partial T}{\partial y} \frac{\partial \psi}{\partial y} + \frac{\partial T}{\partial r} \frac{\partial \psi}{\partial r} \right) drdy + \int_{\gamma_{sf}} \psi h_{c,f} Tr d\gamma + \int_{\gamma_{out}} \psi h_{c,out} Tr d\gamma +$$
$$\int_{\gamma_-} \psi h_{c,-} Tr d\gamma \ . \tag{31}$$

8

The right hand side of equation (30) is linear and the following operator defined on $H_r^1(\omega)$ is introduced:

$$l_T(\psi) = \int_\omega \psi Q r \, dr dy + \int_{\gamma_{sf}} \psi h_{c,f} T_f r \, d\gamma + \int_{\gamma_{out}} \psi h_{c,out} T_{out} r \, d\gamma +$$
$$\int_{\gamma_-} \psi h_{c,-} T_- \, r d\gamma - \int_{\gamma_+} \psi q^+ r \, d\gamma \, . \tag{32}$$

Then, we can define the following problem:

- **Weak thermal model (WT)** : Under the assumptions (TH1)-(TH3), find $T \in H_r^1(\omega)$ such that,

$$a_T(T, \psi) = l_T(\psi) \, , \, \forall \, \psi \in H_r^1(\omega) \, . \tag{33}$$

By using Cauchy-Schwarz inequality, the trace operator properties, and Friedrich's inequality [13, 39], it can be shown that, under the assumptions (TH1)-(TH3), $a_T(T, \psi)$ and $l_T(\psi)$ are continuous on $H_r^1(\omega) \times H_r^1(\omega)$ and $H_r^1(\omega)$, respectively, and $a_T(\psi, \psi)$ is coercive on $H_r^1(\omega) \times H_r^1(\omega)$. Hence the conditions of the Lax-Milgram theorem [13] are satisfied and accordingly the weak thermal model (WT) has a unique solution.

4.3. Weak formulation of the mechanical model

We assume the following hypotheses on the data:

(MH1) The body force density, $\overrightarrow{f_0}$, is such that

$$\overrightarrow{f_0} \in [L_r^2(\omega)]^2 \, .$$

(MH2) The boundary forces $\overrightarrow{g}_+, \overrightarrow{g}_{sf}, \overrightarrow{g}_{out}$ and $\overrightarrow{g}_-$ are such that

$$\overrightarrow{g}_+ \in [L_r^2(\gamma_+)]^2, \, \overrightarrow{g}_{sf} \in [L_r^2(\gamma_{sf})]^2, \, \overrightarrow{g}_{out} \in [L_r^2(\gamma_{out})]^2, \, \overrightarrow{g}_- \in [L_r^2(\gamma_-)]^2.$$

(MH3) The Young's modulus $E(r, y)$, the coefficient of thermal expansion $\alpha(r, y)$, and the Poisson's ratio $\nu(r, y)$ are such that

$$E(r, y) \in L^\infty(\omega) \, , \, E > E_0 > 0 \, ,$$
$$\alpha(r, y) \in L^\infty(\omega) \, , \, \alpha > \alpha_0 > 0 \, ,$$
$$\nu(r, y) \in L^\infty(\omega) \, , \, \nu_0 < \nu < \nu_1 \, , \, \nu_0 > 0 \, ,$$

where E_0, α_0, ν_0 and ν_1 are suitable constants.

Analogously to what has been done for the thermal model, to propose a weak formulation of the mechanical model (18) - (20), in the following we assume sufficient regularity to perform the calculations. Given a function $\overrightarrow{\phi} = (\phi_r, \phi_y)$, we multiply the first equation of (18) by $r\phi_r(r, y)$, the second one by $r\phi_y(r, y)$, we sum both, integrate over ω, apply Green formula and use equation (3) and (20) to obtain

$$\int_\omega \boldsymbol{A}\{\boldsymbol{\varepsilon}(\overrightarrow{u})\} \cdot \{\boldsymbol{\varepsilon}(\overrightarrow{\phi})\} r \, dr dy = \int_\omega (2\mu + 3\lambda)\alpha(T - T_0)\{\boldsymbol{I}\} \cdot \{\boldsymbol{\varepsilon}(\overrightarrow{\phi})\} r \, dr dy +$$
$$\int_\omega (\phi_r f_{0,r} + \phi_y f_{0,y}) \, r \, dr dy + \int_{\gamma_{sf}} \overrightarrow{\phi} \cdot \overrightarrow{g}_{sf} r \, d\gamma + \int_{\gamma_{out}} \overrightarrow{\phi} \cdot \overrightarrow{g}_{out} r \, d\gamma + \tag{34}$$
$$\int_{\gamma_-} \overrightarrow{\phi} \cdot \overrightarrow{g}_- r \, d\gamma + \int_{\gamma_+} \overrightarrow{\phi} \cdot \overrightarrow{g}_+ r \, d\gamma \, , \, \forall \overrightarrow{u}, \overrightarrow{\phi} \in \mathbb{U} \, ,$$

where T is assumed to be the solution of the weak thermal model (WT).

Notice that under assumptions (MH1)-(MH3), and since $T \in H_r^1(\omega)$, all integrals in (34) are well defined for all $\overrightarrow{u}, \overrightarrow{\phi} \in \mathbb{U}$.

The left hand side of equation (34),

$$a_M(\overrightarrow{u}, \overrightarrow{\phi}) = \int_\omega \boldsymbol{A}\{\boldsymbol{\varepsilon}(\overrightarrow{u})\} \cdot \{\boldsymbol{\varepsilon}(\overrightarrow{\phi})\} r \, dr dy \, , \tag{35}$$

9

is bilinear in $\mathbb{V} \times \mathbb{V}$, while the right hand side,

$$l_M[T](\overrightarrow{\phi}) = \int_\omega (2\mu + 3\lambda)\alpha(T - T_0)\{I\} \cdot \{\varepsilon(\overrightarrow{\phi})\} r dr dy + \int_\omega (\phi_r f_{0,r} + \phi_y f_{0,y}) r dr dy +$$
$$\int_{\gamma_{sf}} \overrightarrow{\phi} \cdot \overrightarrow{g}_{sf} r d\gamma + \int_{\gamma_{out}} \overrightarrow{\phi} \cdot \overrightarrow{g}_{out} r d\gamma + \int_{\gamma_-} \overrightarrow{\phi} \cdot \overrightarrow{g}_- r d\gamma + \int_{\gamma_+} \overrightarrow{\phi} \cdot \overrightarrow{g}_+ r d\gamma ,$$

(36)

is linear in $\mathbb{V}$. By using these two operators, the weak formulation of the mechanical problem can be expressed as follows:

- **Weak mechanical problem (WM)** : Let $T \in H_r^1(\omega)$ be the solution of the weak thermal model (WT). Under the assumptions (MH1)-(MH3), find $\overrightarrow{u} \in \mathbb{U}$ such that,

$$a_M(\overrightarrow{u}, \overrightarrow{\phi}) = l_M[T](\overrightarrow{\phi}) , \ \forall \overrightarrow{\phi} \in \mathbb{U} .$$

(37)

By using Lemmas 2.2 and 2.3 of [30], under the assumption ($MH3$), one can show that $a_M(\overrightarrow{u}, \overrightarrow{\phi})$ and $l_M[T](\overrightarrow{\phi})$ are continuous in $\mathbb{V} \times \mathbb{V}$ and $\mathbb{V}$, respectively, and a_M is $\mathbb{U}$-coercive. Hence the conditions of the Lax-Milgram theorem are satisfied and accordingly the weak mechanical formulation (WM) has a unique solution.

Notice that here we could use the principle of superposition: the net displacement at any point in the domain $\overrightarrow{u}$ is the sum of the displacement due to purely mechanical effects $\overrightarrow{u}_M \in \mathbb{U}$ and the displacement due to purely thermal effects $\overrightarrow{u}_T \in \mathbb{U}$:

$$\overrightarrow{u} = \overrightarrow{u}_M + \overrightarrow{u}_T .$$

(38)

Therefore, the problem (WM) could be split in two sub-problems:

- **Weak mechanical problem (WM1)** : Under the assumptions (MH1)-(MH3), find $\overrightarrow{u}_M \in \mathbb{U}$ such that,

$$a_M(\overrightarrow{u}_M, \overrightarrow{\phi}) = l_M[T_0](\overrightarrow{\phi}) , \ \forall \overrightarrow{\phi} \in \mathbb{U} ,$$

(39)

- **Weak mechanical problem (WM2)** : Let $T \in H_r^1(\omega)$ be the solution of the weak thermal model (WT). Under the assumptions (MH1)-(MH3), find $\overrightarrow{u}_T \in \mathbb{U}$ such that,

$$a_M(\overrightarrow{u}_T, \overrightarrow{\phi}) = l_M[T](\overrightarrow{\phi}) - l_M[T_0](\overrightarrow{\phi}) , \ \forall \overrightarrow{\phi} \in \mathbb{U} ,$$

(40)

5. Finite element discretization of the thermo-mechanical model

In this section, we are going to briefly describe the Lagrange finite element method used to approximate the problems (WT), and (WM), ($WM1$) and ($WM2$).

We introduce the n_h- dimensional space $H_{r,h}^1(\omega) \subset H_r^1(\omega)$ and m_h- dimensional space $\mathbb{U}_h \subset \mathbb{U}$,

$$H_{r,h}^1(\omega) = \text{span}\{\psi_{1,h}, \psi_{2,h}, \ldots, \psi_{n_h,h}\} ,$$

(41)

$$\mathbb{U}_h = \text{span}\{\overrightarrow{\phi}_{1,h}, \overrightarrow{\phi}_{2,h}, \ldots, \overrightarrow{\phi}_{m_h,h}\} .$$

(42)

Based on the Galerkin method of weighted residuals [61], we can express the approximated solutions T_h and $\overrightarrow{u}_h$ as follows:

$$T_h = \sum_{i=1}^{n_h} T_h^i \psi_{i,h} ,$$

(43)

$$\overrightarrow{u}_h = \sum_{i=1}^{m_h} u_h^i \overrightarrow{\phi}_{i,h} ,$$

(44)

where T_h^i and u_h^i are the nodal temperature and nodal displacement, respectively, and the basis functions $\psi_{i,h}$ and $\overrightarrow{\phi}_{i,h}$ are piecewise polynomial of degree $p \geq 1$ in (r, y) space.

Therefore, the approximation of the problem (WT) in the finite dimensional space $H_{r,h}^1$ can be stated as,

10

- **Problem** $(WT)_h$: Under the assumptions $(TH1) - (TH3)$, find $T_h \in H^1_{r,h}(\omega)$ such that,

$$a_T(T_h, \psi_h) = l_T(\psi_h) , \ \forall \psi_h \in H^1_{r,h}(\omega) . \tag{45}$$

Similarly, the approximation of the problems (WM), $(WM1)$ and $(WM2)$ in the finite dimensional space $\mathbb{U}_h$ can be stated as:

- **Problem** $(WM)_h$: Let $T_h \in H^1_{r,h}(\omega)$, be the solution of the discretized thermal model $(WT)_h$. Under the assumptions $(MH1) - (MH3)$, find $\overrightarrow{u}_h \in \mathbb{U}_h$ such that,

$$a_M(\overrightarrow{u}_h, \overrightarrow{\phi}_h) = l_M[T_h](\overrightarrow{\phi}_h) , \ \forall \overrightarrow{\phi}_h \in \mathbb{U}_h . \tag{46}$$

- **Problem** $(WM1)_h$: Under the assumptions $(MH1) - (MH3)$, find $\overrightarrow{u}_{M,h} \in \mathbb{U}_h$ such that,

$$a_M(\overrightarrow{u}_{M,h}, \overrightarrow{\phi}_h) = l_M[T_0](\overrightarrow{\phi}_h) , \ \forall \overrightarrow{\phi}_h \in \mathbb{U}_h . \tag{47}$$

- **Problem** $(WM2)_h$: Let $T_h \in H^1_{r,h}(\omega)$, be the solution of the discretized thermal model $(WT)_h$. Under the assumptions $(MH1) - (MH3)$, find $\overrightarrow{u}_{T,h} \in \mathbb{U}_h$ such that,

$$a_M(\overrightarrow{u}_{T,h}, \overrightarrow{\phi}_h) = l_M[T_h](\overrightarrow{\phi}_h) - l_M[T_0](\overrightarrow{\phi}_h) , \ \forall \overrightarrow{\phi}_h \in \mathbb{U}_h . \tag{48}$$

6. Model order reduction

In this section, we present our MOR framework. Firstly, we introduce the parameter space related to the problem under investigation (Sec. 6.1). Then, in Sec. 6.2, we describe the POD algorithm that is used for the construction of reduced basis space as well as the two methods adopted for the computation of the reduced degrees of freedom, Galerkin projection (G) and Artificial Neural Network (ANN). Finally, in Sec. 6.3, we show some numerical tests with the aim to validate our approach. The MOR computations have been carried out using RBniCS [28, 46], an in-house open source python library employing several reduced order techniques based on FEniCS [1, 19], and PyTorch [40, 42], a python machine learning library.

6.1. Parameter space

Let $\mathbb{P} \subset \mathbb{R}^d$ be the parameter space having dimensionality d with $\Xi \in \mathbb{P}$ a tuple of parameters. For the problem of the hearth blast furnace, the relevant parameters are related both to the physical properties and the geometry of the domain ω. The physical parameters are the thermal conductivity of the material, k, the thermal expansion coefficient, α, the Young modulus, E, and the Poisson's ratio, ν. On the other hand, the geometric parameters are the diameter of each section of the hearth D_0, D_1, D_2, D_3, D_4, and the thickness of each section of the hearth t_0, t_1, t_2, t_3, t_4 (see Figure 4). So for the problem under consideration, in the most general case (i.e., when all the parameters are considered), we have $\Xi = \{\Xi_p, \Xi_g\}$ where $\Xi_p = \{k, \alpha, E, \nu\} \in \mathbb{P}_p \subset \mathbb{R}^4$ is the physical parameters tuple and $\Xi_g = \{D_0, D_1, D_2, D_3, D_4, t_0, t_1, t_2, t_3, t_4\} \in \mathbb{P}_g \subset \mathbb{R}^{10}$ is the geometric parameters tuple, and $d = 14$.

Let us consider a geometrical parameters tuple $\bar{\Xi}_g$ and the corresponding domain $\hat{\omega} = \omega(\bar{\Xi}_g)$. We refer to $\hat{\omega}$ as the reference domain. The domain $\hat{\omega}$ is divided into n_{su} non-overlapping triangular subdomains (see, e.g., [32, 48]), i.e.

$$\hat{\omega} = \bigcup_{i=1}^{n_{su}} \hat{\omega}_i , \ \hat{\omega}_i \cap \hat{\omega}_j = \emptyset \text{ for } i \neq j , \ 1 \leq i, j \leq n_{su} . \tag{49}$$

For each of the subdomains $\hat{\omega}_i$, one can consider an invertible mapping $\boldsymbol{F}_i$,

$$\boldsymbol{F}_i : \hat{\omega}_i \times \mathbb{P}_g \rightarrow \omega_i , \tag{50}$$

of the form

$$\overrightarrow{x} = \boldsymbol{F}_i(\overrightarrow{\hat{x}}, \Xi_g) = \boldsymbol{G}_{F,i}(\Xi_g)\overrightarrow{\hat{x}} + \overrightarrow{c}_{F,i}(\Xi_g); \ , \ \forall \overrightarrow{\hat{x}} \in \hat{\omega}_i , \forall \overrightarrow{x} \in \omega_i(\Xi_g) , \tag{51}$$

where

$$\boldsymbol{G}_{F,i} = \begin{bmatrix} G_{F,i,11} & G_{F,i,12} \\ G_{F,i,21} & G_{F,i,22} \end{bmatrix} , \ \overrightarrow{x} = \{r \ y\}^T , \ \overrightarrow{\hat{x}} = \{\hat{r} \ \hat{y}\}^T , \overrightarrow{c}_{F,i} = \{c_{F,i,1} \ c_{F,i,2}\}^T . \tag{52}$$

Equation (51) highlights that the Jacobian matrix $\boldsymbol{G}_{F,i}$ and translation vector $\overrightarrow{c}_{F,i}$ are dependent only on the geometric parameters tuple Ξ_g and do not vary over a given subdomain. In the following, the domains ω will be the image by eq. (51) of the reference domain for the tuples of geometric parameters considered.
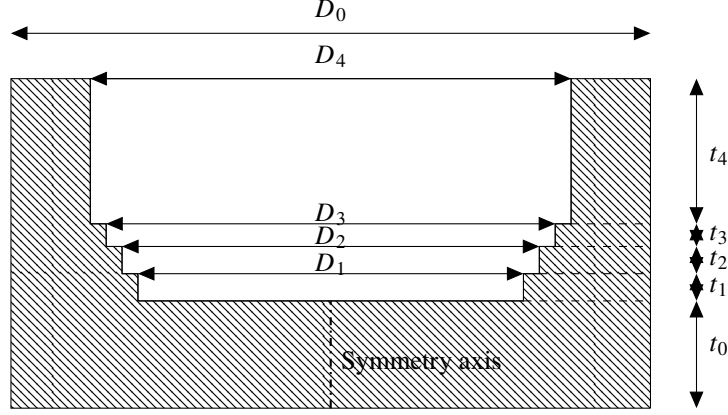
Figure 4: Hearth geometric parameters of ω: diameters D_0, D_1, D_2, D_3, D_4 and thicknesses t_0, t_1, t_2, t_3, t_4.

6.2. Main ingredients of MOR

The basic idea of MOR is the assumption that solutions live in a low dimensional manifold. Thus, any solution can be approximated based on a reduced number of global basis functions.

We seek the reduced basis approximations $T_h^{rb} \in H_{r,h}^{1,rb}(\omega)$ and $\overrightarrow{u}_h^{rb} \in \mathbb{U}_h^{rb}$ of $T_h \in H_{r,h}^1(\omega)$ and $\overrightarrow{u}_h \in \mathbb{U}_h$, respectively. The reduced basis spaces $H_{r,h}^{1,rb}(\omega) \subset H_{r,h}^1(\omega)$ and $\mathbb{U}_h^{rb} \subset \mathbb{U}_h$ are given by,

$$H_{r,h}^{1,rb}(\omega) = \operatorname{span}\{\psi_h^1, \ldots, \psi_h^{N_T}\},$$
$$\mathbb{U}_h^{rb} = \operatorname{span}\{\overrightarrow{\phi}_h^1, \ldots, \overrightarrow{\phi}_h^{N_M}\},$$

where $N_M << m_h$ and $N_T << n_h$ are the number of basis functions forming the reduced basis spaces $H_{r,h}^{1,rb}(\omega)$ and $\mathbb{U}_h^{rb}$, respectively. Then we can represent $\overrightarrow{u}_h^{rb}$ and T_h^{rb} by

$$T_h^{rb} = \sum_{i=1}^{N_T} \zeta_T^i \psi_h^i, \tag{53}$$

$$\overrightarrow{u}_h^{rb} = \sum_{i=1}^{N_M} \zeta_M^i \overrightarrow{\phi}_h^i, \tag{54}$$

where $\{\zeta_T^i\}_{i=1}^{N_T}$ and $\{\zeta_M^i\}_{i=1}^{N_M}$ are the temperature and displacement degrees of freedom, respectively.

We also construct the reduced basis spaces for displacement fields $\overrightarrow{u}_{T,h}$ and $\overrightarrow{u}_{M,h}$, introduced in (47) and (48), as,

$$\mathbb{U}_{T,h}^{rb} = \operatorname{span}\{\overrightarrow{\phi}_{T,h}^1, \ldots, \overrightarrow{\phi}_{T,h}^{N_{M,T}}\},$$
$$\mathbb{U}_{M,h}^{rb} = \operatorname{span}\{\overrightarrow{\phi}_{M,h}^1, \ldots, \overrightarrow{\phi}_{M,h}^{N_{M,M}}\}.$$

So, the reduced basis approximations $\overrightarrow{u}_{M,h}^{rb} \in \mathbb{U}_{M,h}^{rb}$ of $\overrightarrow{u}_{M,h} \in \mathbb{U}_h$ and $\overrightarrow{u}_{T,h}^{rb} \in \mathbb{U}_{T,h}^{rb}$ of $\overrightarrow{u}_{T,h} \in \mathbb{U}_h$ can be represented as,

$$\overrightarrow{u}_{M,h}^{rb} = \sum_{i=1}^{N_{M,M}} \zeta_{M,M}^i \overrightarrow{\phi}_{M,h}^i, \overrightarrow{u}_{T,h}^{rb} = \sum_{i=1}^{N_{M,T}} \zeta_{M,T}^i \overrightarrow{\phi}_{T,h}^i. \tag{55}$$

6.2.1. POD algorithm

In the literature, one can find several techniques to generate the reduced basis spaces, e.g. Proper Orthogonal Decomposition (POD), the Proper Generalized Decomposition (PGD) and the Reduced Basis (RB) with a greedy sampling strategy. See, e.g., [3, 11, 24, 28, 43]. In this work, the reduced basis spaces are constructed by POD that is able to capture the "dominant" modes by exploiting the information contained in the full order snapshots.

We are going to describe the procedure for the computation of the reduced basis space $H_{r,h}^{1,rb}(\omega)$. The reduced basis spaces $\mathbb{U}_h^{rb}$, $\mathbb{U}_{T,h}^{rb}$ and $\mathbb{U}_{M,h}^{rb}$ are constructed in an analogous way. First, n_s parameter tuples, $\{\Xi_k\}_{k=1}^{n_s}$, are considered that form the training set. We compute the snapshots $T_h(\Xi_k)$ related to each parameter tuple in the training set. Then a matrix $\boldsymbol{C}_T \in \mathbb{R}^{n_s \times n_s}$ is constructed,

$$(\boldsymbol{C}_T)_{kl} = <T_h(\Xi_k), T_h(\Xi_l)>_{H_{r,h}^1(\hat{\omega})} , \ 1 \le k, l \le n_s , \tag{56}$$

where transformation (51) is considered. Next, N_T largest eigenvalues $\{\theta_T^i\}_{i=1}^{N_T}$ of the matrix $\boldsymbol{C}_T$, sorted in descending order, $\theta_T^1 \ge \theta_T^2 \ge \ldots \ge \theta_T^{N_T}$, and corresponding eigenvectors $\{\boldsymbol{V}_T^i\}_{i=1}^{N_T}, \boldsymbol{V}_T^i \in \mathbb{R}^{n_s}$, are computed,

$$\boldsymbol{C}_T \boldsymbol{V}_T^i = \theta_T^i \boldsymbol{V}_T^i . \tag{57}$$

The reduced basis are then given by

$$\psi_h^i = \frac{\sum\limits_{k=1}^{n_s} (\boldsymbol{V}_T^i)_k T_h(\Xi_k)}{|| \sum\limits_{k=1}^{n_s} (\boldsymbol{V}_T^i)_k T_h(\Xi_k)||_{H_{r,h}^1(\hat{\omega})}} , \ 1 \le i \le N_T . \tag{58}$$

In order to determine the admissibility of a given eigenvector into the POD space, we refer to the following criterion

$$\frac{\theta_T^i}{\theta_T^1} \ge 1e - 4 . \tag{59}$$

In the following subsections, we describe two different approaches for the computation of the degrees of freedom: Galerkin projection (G) and Artificial Neural Network (ANN).

6.2.2. Galerkin projection

Here we choose to consider $(WM1)_h$ and $(WM2)_h$ in the place of $(WM)_h$ because the displacements due to purely mechanical effects and those due to purely thermal effects may have different characteristic scales. So treating these systems separately ensures that the system with bigger scale effects does not dominate the global system, avoiding a significant impact on the accuracy of MOR: see, e.g., [31, 51, 60].

We consider an affine parametric dependence, i.e. the bilinear forms $a_T(\cdot, \cdot; \Xi)$ and $a_M(\cdot, \cdot; \Xi)$ are expressed as weighted sum of n_{a_T} and n_{a_M} parameter independent bilinear forms. Similarly, the linear forms $l_T(\cdot; \Xi)$ and $l_M[T](\cdot; \Xi)$ are expressed as weighted sum of n_{l_T} and n_{l_M} parameter independent linear forms. We have:

$$a_T(T, \psi; \Xi) = \sum_{i=1}^{n_{a_T}} \theta_{a_T,i}(\Xi) a_{T,i}(T, \psi; \bar{\Xi}) ,$$

$$l_T(\psi; \Xi) = \sum_{i=1}^{n_{l_T}} \theta_{l_T,i}(\Xi) l_{T,i}(\psi; \bar{\Xi}) , \tag{60}$$

and

$$a_M(\vec{u}, \vec{\phi}; \Xi) = \sum_{i=1}^{n_{a_M}} \theta_{a_M,i}(\Xi) a_{M,i}(\vec{u}, \vec{\phi}; \bar{\Xi}) ,$$

$$l_M[T](\vec{\phi}; \Xi) = \sum_{i=1}^{n_{l_M}} \theta_{l_M,i}(\Xi) l_{M,i}[T](\vec{\phi}; \bar{\Xi}) . \tag{61}$$

The affine expansion of operators is essentially a change of variables and has been widely addressed in the literature: see, e.g., [11, 24, 28]. The affinity assumption is particularly important as it leads to considerable efficiency. This is mainly due to the fact that the evaluation of bilinear forms, $a_{M,i}(\vec{u}, \vec{\phi})$ and $a_{T,i}(T, \psi)$, and linear forms, $l_{T,i}(\psi)$ and $l_{M,i}[T](\vec{\phi})$ are not required for each new tuple of parameters.
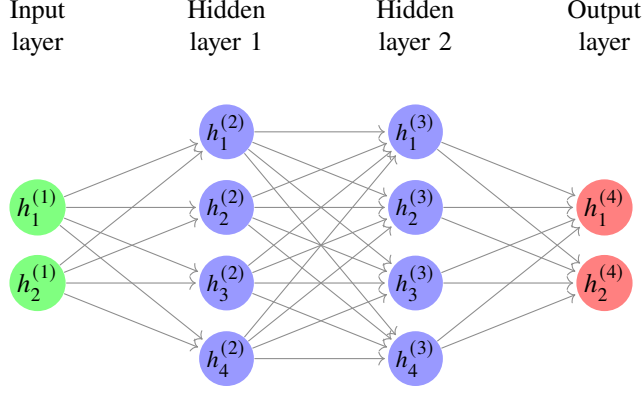
13

Figure 5: Sketch of a feed-forward ANN with 2 hidden layers.

So for what concerns the model $(WT)_h$, the bilinear form $a_{T,h} : H_{r,h}^1(\omega) \times H_{r,h}^1(\omega) \to \mathbb{R}$ is restricted to the reduced basis space as $a_{T,h}^{rb} : H_{r,h}^{1,rb}(\omega) \times H_{r,h}^{1,rb}(\omega) \to \mathbb{R}$. In the same way, the linear form $l_{T,h} : H_{r,h}^1(\omega) \to \mathbb{R}$ is restricted to the reduced basis space as $l_{T,h}^{rb} : H_{r,h}^{1,rb}(\omega) \to \mathbb{R}$. So the reduced basis approximation T_h^{rb} at a given parameter tuple Ξ^* is obtained by solving

$$a_{T,h}^{rb}(T_h^{rb}, \psi_h^{rb}; \Xi^*) = l_{T,h}^{rb}(\psi_h^{rb}; \Xi^*) \, , \; \forall \psi_h^{rb} \in H_{r,h}^{1,rb}(\omega) \, . \tag{62}$$

On the other hand, for what concerns the model $(WM1)_h$, the bilinear form $a_{M,h} : \mathbb{U}_h \times \mathbb{U}_h \to \mathbb{R}$ is restricted to the reduced basis space as $a_{M,h}^{rb} : \mathbb{U}_{M,h}^{rb} \times \mathbb{U}_{M,h}^{rb} \to \mathbb{R}$. The linear form $l_{M,h} : \mathbb{U}_h \to \mathbb{R}$ is restricted to the reduced basis space as $l_{M,h}^{rb} : \mathbb{U}_{M,h}^{rb} \to \mathbb{R}$. So the reduced basis approximation $\overrightarrow{u}_{M,h}^{rb}$ at a given parameter tuple Ξ^* is obtained by solving,

$$a_{M,h}^{rb}(\overrightarrow{u}_{M,h}^{rb}, \overrightarrow{\phi}_{M,h}^{rb}; \Xi^*) = l_{M,h}^{rb}[T_0](\overrightarrow{\phi}_{M,h}^{rb}; \Xi^*) \, , \; \forall \overrightarrow{\phi}_{M,h}^{rb} \in \mathbb{U}_{M,h}^{rb} \, . \tag{63}$$

Similarly, for the model $(WM2)_h$ the bilinear form $a_{M,h} : \mathbb{U}_h \times \mathbb{U}_h \to \mathbb{R}$ is restricted to the reduced basis space as $a_{M,h}^{rb} : \mathbb{U}_{T,h}^{rb} \times \mathbb{U}_{T,h}^{rb} \to \mathbb{R}$. The linear form $l_{M,h} : \mathbb{U}_h \to \mathbb{R}$ is restricted to the reduced basis space as $l_{M,h}^{rb} : \mathbb{U}_{T,h}^{rb} \to \mathbb{R}$. So, the reduced basis approximation $\overrightarrow{u}_{T,h}^{rb}$ at a given parameter Ξ^* is obtained by solving,

$$a_{M,h}^{rb}(\overrightarrow{u}_{T,h}^{rb}, \overrightarrow{\phi}_{T,h}^{rb}; \Xi^*) = l_{M,h}^{rb}[T_h^{rb}](\overrightarrow{\phi}_{T,h}^{rb}; \Xi^*) - l_{M,h}^{rb}[T_0](\overrightarrow{\phi}_{T,h}^{rb}; \Xi^*) \, , \; \forall \overrightarrow{\phi}_{T,h}^{rb} \in \mathbb{U}_{T,h}^{rb} \, . \tag{64}$$

6.2.3. Artificial Neural Network

Artificial Neural Network (ANN) is a computational model that takes inspiration from the human brain consisting of an interconnected network of simple processing units that can learn from experience by modifying their connections (see, e.g., [25, 47]).

Recently, the application of deep learning methods to partial differential equations has shown promising capabilities: see, e.g., [36, 37, 44, 16, 45, 54, 4]. Concerning the application of the ANN approach in a MOR context, the reader is referred, e.g., to [27, 49, 56, 16, 41, 58, 17, 38]. We highlight that, unlike the Galerkin projection, ANN is a data-driven approach, i.e. based only on data and does not require the knowledge of the original equations describing the system. It is also non-intrusive, in the sense that no modification of the simulation software is required.

In this work, we use a feed-forward ANN consisting of input layer, two hidden layers whose depth H (i.e., the number of neurons constituting the hidden layer) is determined by trial and error [27], and output layer. See Figure 5 for an illustrative representation of a feed-forward ANN. The weights as well as the biasing parameters of the network are iteratively adjusted by the backpropagation process using an optimization algorithm [34]. Concerning the activation function, we consider for hidden layers the Sigmoid function [59] whilst for the initial and final layer we use the identity function.

Unlike what done for the Galerkin projection approach, concerning the mechanical problem, we consider the model $(WM)_h$. This choice is due to the fact that ANN suffers from high offline cost because of the training phase, so it is beneficial to train one only model instead of training two models.

We consider N_t^T parameter tuples $\{\Xi_k\}_{k=1}^{N_t^T}$ and compute the temperature field $T_h(\Xi_k)$ by solving problem $(WT1)_h$ at each parameter tuple Ξ_k. Next, the temperature field $T_h(\Xi_k)$ is projected on the reduced basis space so to obtain the projected solution $T_h^\pi(\Xi_k)$ and corresponding degrees of freedom $\zeta_{T,\pi}(\Xi_k)$:

$$T_h^\pi(\Xi_k) = \underset{\psi_h^{rb} \in H_{r,h}^{1,rb}(\omega)}{\arg\min} ||T_h(\Xi_k) - \psi_h^{rb}||_{H_{r,h}^1(\omega)} = \sum_{i=1}^{N_T} \zeta_{T,\pi}^i(\Xi_k)\psi_h^i . \tag{65}$$

Similarly, we consider N_t^M parameter tuples $\{\Xi_k\}_{k=1}^{N_t^M}$ and compute the displacement fields $\overrightarrow{u}_h(\Xi_k)$ by solving problem $(WM)_h$ at each parameter tuple Ξ_k. Next, the displacement field $\overrightarrow{u}_h(\Xi_k) \in \mathbb{U}_h$ is projected on the reduced basis space so to obtain the projected solution $\overrightarrow{u}_h^\pi(\Xi_k)$ and corresponding degrees of freedom $\zeta_{M,\pi}(\Xi_k)$:

$$\overrightarrow{u}_h^\pi(\Xi_k) = \underset{\overrightarrow{\phi}_h^{rb} \in \mathbb{U}_h^{rb}}{\arg\min} ||\overrightarrow{u}_h(\Xi_k) - \overrightarrow{\phi}_h^{rb}||_{\mathbb{U}_h} = \sum_{i=1}^{N_M} \zeta_{M,\pi}^i(\Xi_k)\overrightarrow{\phi}_h^i . \tag{66}$$

So we consider two collections of (known) training input-desidered output pairs, $\{\Xi_k, \zeta_{T,\pi}(\Xi_k)\}_{k=1}^{N_t^T}$ and $\{\Xi_k, \zeta_{M,\pi}(\Xi_k)\}_{k=1}^{N_t^M}$. The goal is to approximate the functions f_T and f_M that map these training input-desidered output pairs. After training the two ANNs, we consider them as black boxes that can then be used to compute the POD coefficients related to a new parameter instance Ξ^*.

We split the full order data into two parts: one to be used for training and one to be used for validation. While the training data are used to adjust weights and biasing parameters of the ANN, the validation data are used to measure its accuracy. A common issue is that ANN may perform better on training data but may not perform well on data other than training data. To avoid this overfitting phenomenon, we use the early stopping criteria [25]: the training is stopped when the the mean squared error

$$\begin{aligned}
\epsilon_T &= \frac{\sum\limits_{i=1}^{N_T} \left(\zeta_{T,\pi}^i(\Xi_k) - \zeta_T^i(\Xi_k)\right)^2}{N_T} , \\
\epsilon_M &= \frac{\sum\limits_{i=1}^{N_M} \left(\zeta_{M,\pi}^i(\Xi_k) - \zeta_M^i(\Xi_k)\right)^2}{N_M} ,
\end{aligned} \tag{67}$$

as measured on validation data starts to increase.

6.3. MOR results

The coordinates of the 12 vertices constituting the reference domain are reported in Table 1.

r	0	7.05	7.05	5.30	5.30	4.95	4.95	4.6	4.6	4.25	4.25	0
y	0	0	7.265	7.265	4.065	4.065	3.565	3.565	2.965	2.965	2.365	2.365

Table 1: coordinates (in m) of the vertices of domain $\hat{\omega}$ (see Figure 6).

We set $n_{su} = 30$ (see Figure 6a). The considered mesh is compliant with the triangular subdomains and contains 8887 triangular elements and 4608 vertices (see Figure 6b). A proper domain decomposition ensures that a suitable mesh can be used for the discretization on each of the subdomains and also throughout one subdomain and the other. As shown in Figure 7, an improper domain decomposition could generate regions with poor mesh quality. Another issue that might arise from an improper domain decomposition is that, under the variation of the geometrical parameters, poor mesh quality might occur in some regions: an example is showed in Figure 8.

The minimum and maximum mesh size, that is measured as distance between vertices of an element of the mesh, are 0.047m and 0.16m respectively. The quality of each mesh element, q_e, could be estimated by using the following formula [57]:

$$q_e = \frac{4\sqrt{3}A}{l_1^2 + l_2^2 + l_3^2} , \tag{68}$$
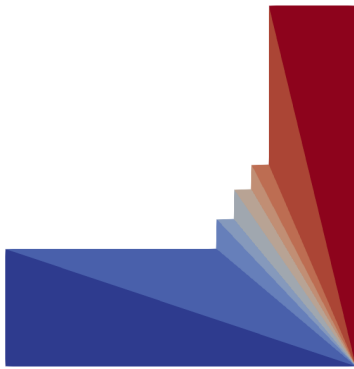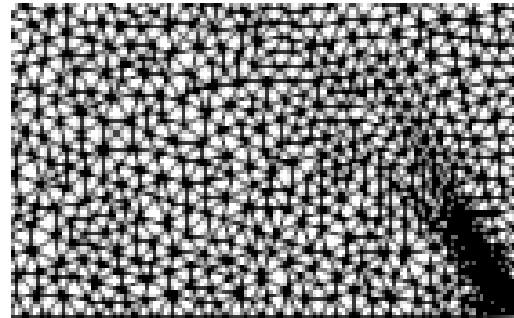
(a) Subdomains decomposition.
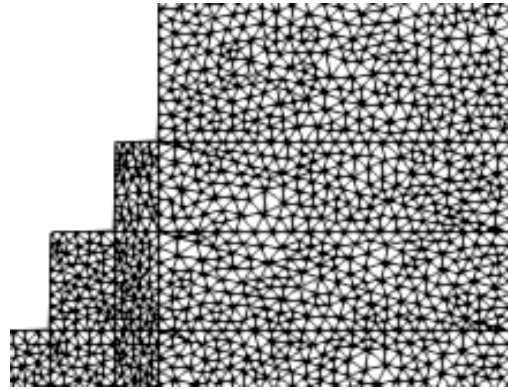
(b) Close up of the mesh.

Figure 6: Discretization of the domain $\hat{\omega}$.

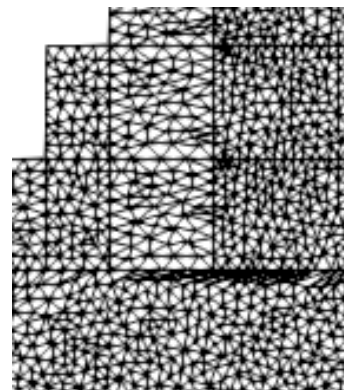(a) Subdomains decomposition.

(b) Close up of the mesh at bottom right.

Figure 7: Improper domain decomposition: poor mesh quality at bottom right.

(a) Subdomains decomposition.

(b) Close up of the region affected by poor mesh quality.

Figure 8: Improper domain decomposition: poor mesh quality under variation of the diameter D_4.

where A is the area of the element, and l_1, l_2 and l_3 are the lengths of its three edges. The minimum value of q_e was 0.25, that is sufficiently far from zero.

Notice that we use a coarser mesh with respect to the one used for the FOM benchmark tests in Appendix A. Such a choice is justified by the fact that the FOM solution is required to be solved at many parameters values, so using a fine mesh can be very costly and make prohibitive the collection of the high-fidelity database.

The ranges of physical and geometrical parameters for training and testing are reported in Table 2. The sampling is carried out by using a Latin Hypercube Sampling (LHS) approach [33] which is a statistical method for generating near-random samples of parameter values from a multidimensional distribution. LHS divides the parameter space into equal partitions and samples parameters from each partition. In this manner, it is ensured that the patterns from entire parameter space are represented. The process has been repeated multiple times in order to ensure that random nature of samplings do not affect the final result. ANN has been trained by using the 70% of the total data provided by the full order model whilst the remaining 30% is used for the validation.

Parameter	Minimum value	Maximum value
t_0	2.3	2.4
t_1	0.5	0.7
t_2	0.5	0.7
t_3	0.4	0.6
t_4	3.05	3.35
D_0	13.5	14.5
D_1	8.3	8.7
D_2	8.8	9.2
D_3	9.8	10.2
D_4	10.4	10.8
k	9.8	10.2
μ	1.9e9	2.5e9
λ	1.2e9	1.8e9
α	0.8e-6	1.2e-6

Table 2: Parameters ranges used for MOR training and testing.

The accuracy of our MOR approach is quantified by the relative error defined as follows

$$\epsilon_{rel,X_h} = \frac{||X_h - X_h^{rb}||}{||X_h||}, \tag{69}$$

where X_h and X_h^{rb} are the finite element solution and the corresponding reduced basis solution, respectively. We consider the projection error between the finite element solution X_h and its projection on the reduced basis space X_h^{π},

$$\epsilon_{proj,X_h} = \frac{||X_h - X_h^{\pi}||}{||X_h||}, \tag{70}$$

as benchmark for the relative error. $|| \cdot ||$ is the relevant norm ($|| \cdot ||_{H_{r,h}^1(\omega)}$ and $|| \cdot ||_{\mathbb{U}_h}$).

6.3.1. Thermal model

We consider four numerical experiments that differ in terms of kind (physical and/or geometrical) and number of the parameters considered:

- *Numerical experiment (i)*: 1 physical parameter: $\Xi = \{k\}$.

- *Numerical experiment (ii)*: 1 physical parameter and 3 geometric parameters: $\Xi = \{k, t_0, D_2, D_4\}$.

- *Numerical experiment (iii)*: 1 physical parameter and 6 geometric parameters: $\Xi = \{k, t_0, t_2, t_4, D_0, D_2, D_4\}$.

- *Numerical experiment (iv)*: 1 physical parameter and all (10) geometric parameters: $\Xi = \{k, t_0, t_1, t_2, t_3, t_4, D_0, D_1, D_2, D_3, D_4\}$.

Table 3 shows the number of samples provided by the full order model, n_{tr}, as well as the number of samples used for training and testing of ANN. Regarding the computation of POD space, for *numerical experiment (i)*, 50 FOM snapshots were considered while for the other ones 1000. The eigenvalues decay is shown in Figure 9. We see that the decay related to the numerical experiment (iv) is the slowest. This is due to the fact that in the numerical experiment (iv) we consider a larger number of parameters, so the system exhibits a greater complexity, and the modal content is more wide.

Figure 10 shows the relative error (69) both for POD-ANN, related to different values n_{tr} and depth of hidden layers H, and POD-G. We also report the projection error (70). We observe that the performance of the POD-ANN method crucially depends on the values of n_{tr} and H. As expected, if we expand the training set and increase the depth of hidden layers, we obtain more accurate predictions when the number of parameters considered starts to get significative (numerical experiments (iii) and (iv)). Unlike [27], we observe that the POD-G method results to be in general more accurate than the POD-ANN method. This could be justified by considering that in the nonlinear framework, investigated in [27], the affine expansion could not be enforced and an Empirical Interpolation Method (EIM) [7] is used within the POD-G approach. Its implementation introduces interpolation error during the assembling of the reduced equations system by significantly affecting the accuracy of the POD-G method.

Illustrative representations of the computed FOM and MOR are displayed in Figure 11 related to the numerical experiment (iv) for the parameters tuple

$$\Xi = \{2.365, 0.6, 0.6, 0.5, 3.2, 14.10, 8.50, 9.2, 9.9, 10.6, 10\} .$$

We use 4 POD basis. The POD-ANN solution was computed with $n_{tr} = 4500$ and $H = 70$. As we can see from Figure 11, both MOR approaches are able to provide a good reconstruction of the temperature field.

We conclude by proving some information about the efficiency of our MOR approach. We report in Table 4 some estimations related to the offline time for all the numerical experiments carried out. We observe that the time taken by POD for numerical experiments (ii)-(iv) is much larger than the numerical experiment (i). This is fully justified by the fact that for the numerical experiments (ii)-(iv) we consider a larger number of snapshots (1000 instead of 50 as discussed above) for the computation of the reduced space. On the other hand, it should also be noted that the ANN training is faster for the numerical experiment (i) where only physical parameters are involved. This could be attributed to the fact that the introduction of geometric parameters increases the complexity of the input-output map that ANN is expected to learn. If on one hand the offline cost of the POD-G method is most composed of time taken by the computation of the snapshots from which the reduced space is extracted and the time taken by the computation of the POD modes, on the other hand the one related to the POD-ANN method is mainly associated to the computation of training data. So, when the parameter space is large (as for the numerical experiments (ii)-(iv)), the total offline cost of the POD-ANN method could be importantly greater than the one related to the POD-G method. We report in Table 5 the online time related to the POD-G and POD-ANN methods for all the numerical experiments carried out. As can be seen, the online time of POD-G method increases significantly in presence of geometric parameters by moving from $7e-4$ s (numerical experiment (i)) to $1.3/1.5e-2$ s (numerical experiments (ii)-(iv)). On the other hand, the time taken by POD-ANN online stage remains relatively constant for all the numerical experiments under investigation, around $5e-4$. So the computational efficiency of POD-ANN is much higher, of almost two order of magnitude, than POD-G when geometrical parametrization is considered.

	n_{tr}	Training	Testing
Numerical experiment (i)	100	70	30
Numerical experiment (ii)	500	350	150
	1500	1050	450
Numerical experiment (iii)	2000	1400	600
	2500	1750	750
Numerical experiment (iv)	3500	2450	1050
	4500	3150	1350

Table 3: Thermal model: number of total samples n_{tr} by FOM and number of samples used for training and testing of ANN.
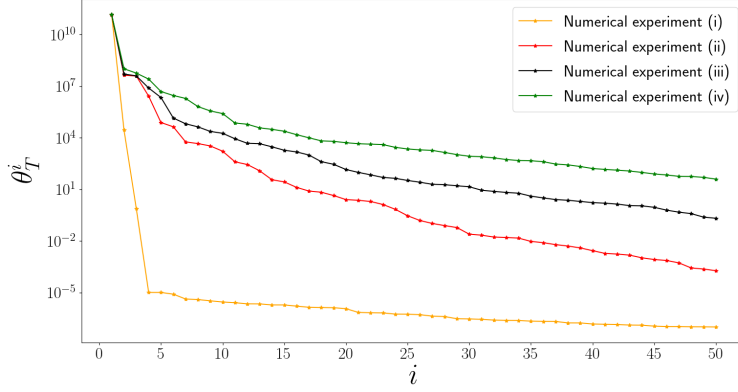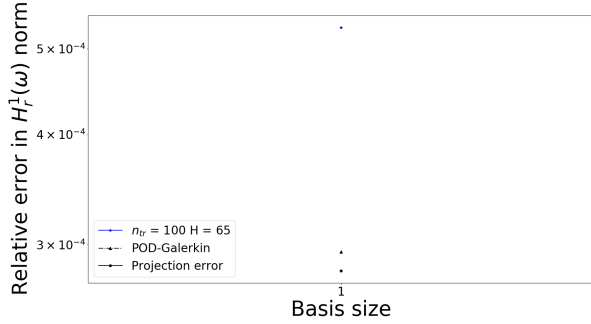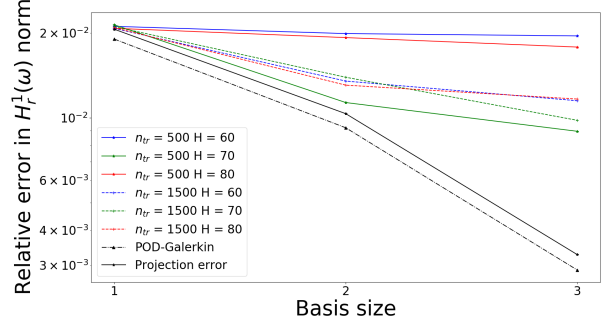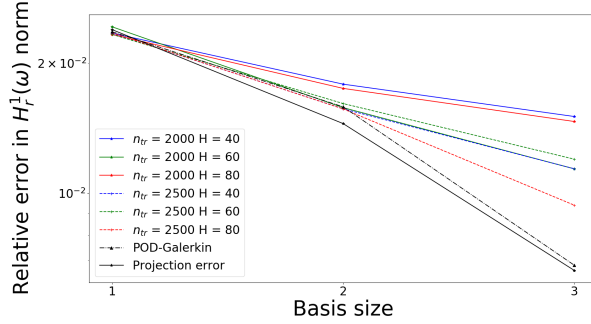
Figure 9: Thermal model: plot of the eigenvalues $\{\theta_T^i\}_{i=1}^{50}$ sorted in descending order for all the numerical experiments considered.
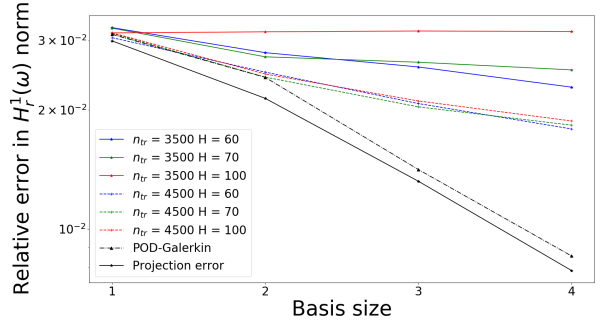

(a) Numerical experiment (i).

(b) Numerical experiment (ii).

(c) Numerical experiment (iii).

(d) Numerical experiment (iv).

Figure 10: Thermal model: error analysis for POD-G and POD-ANN for all the numerical experiments carried out.

	t_{off}^{POD-G}	$t_{off}^{POD-ANN}$	t_{POD}	t_{tr}	t_{FOM}	t_{proj}
Numerical experiment (i)	≈ 5	$\approx 1.2e1$	8.4e-1	2.6e-1		6.0e-4
Numerical experiment (ii)	$\approx 9e1$	$\approx 1.3e2$	1.2e1	5.9e-1	8e-2	7.5e-4
Numerical experiment (iii)	$\approx 9e1$	$\approx 3.7e2$	1.2e1	7.4e1		7.1e-4
Numerical experiment (iv)	$\approx 9e1$	$\approx 5.0e2$	1.2e1	4.5e1		7.3e-4

Table 4: Thermal model: time (in s) taken by (i) the entire offline stage (t_{off}), (ii) the computation of the POD modes (t_{POD}), (iii) the training of ANN (t_{tr}), (iv) the computation of a FOM solution (t_{FOM}) and (v) projection of a FOM solution on the POD space (t_{proj}). Concerning POD-ANN, we use $n_{tr} = 100$, $H = 65$ for the numerical experiment (i), $n_{tr} = 500$, $H = 70$ for the numerical experiment ii), $n_{tr} = 2500$, $H = 80$ for the numerical experiment (iii) and $n_{tr} = 4500$, $H = 70$ for the numerical experiment (iv).

	Basis size	POD-G	POD-ANN
Numerical experiment (i)	1	7.0e-4	4.9e-4
Numerical experiment (ii)	3	1.3e-2	4.8e-4
Numerical experiment (iii)	3	1.5e-2	4.9e-4
Numerical experiment (iv)	4	1.3e-2	5.1e-4

Table 5: Thermal model: online time (in s) for all the numerical experiments under investigation. Concerning POD-ANN, we use $n_{tr} = 100, H = 65$ for the numerical experiment (i), $n_{tr} = 500, H = 70$ for the numerical experiment ii), $n_{tr} = 2500, H = 80$ for the numerical experiment (iii) and $n_{tr} = 4500, H = 70$ for the numerical experiment (iv).

(a) FOM solution   (b) POD-G solution   (c) POD-ANN solution
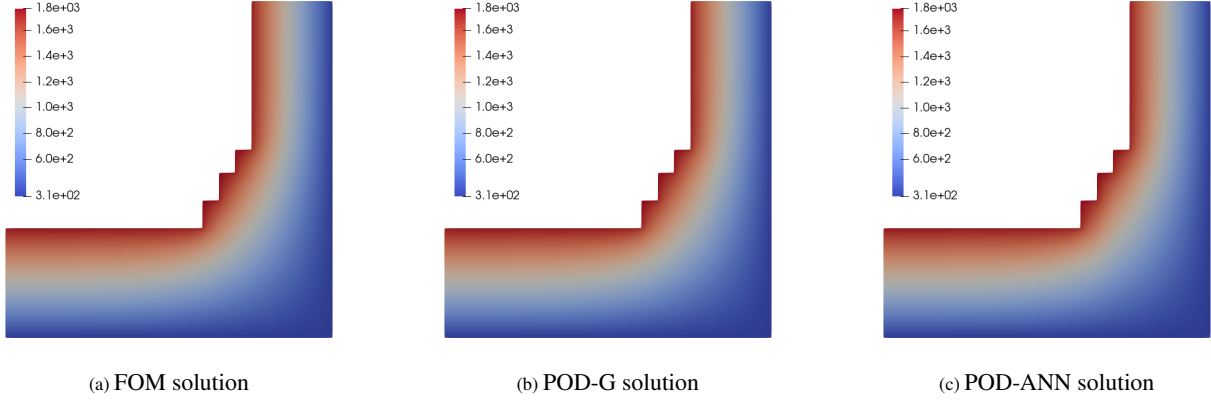
Figure 11: Thermal model: comparison between the temperature field (in K) computed by the FOM and by the POD-G and POD-ANN methods related to the numerical experiment (iv) for $\Xi = \{2.365, 0.6, 0.6, 0.5, 3.2, 14.10, 8.50, 9.2, 9.9, 10.6, 10\}$. We consider 4 POD modes. For POD-ANN, we set $n_{tr} = 4500$ and $H = 70$.

6.3.2. Mechanical model

We remark that for POD-ANN we refer to the $(WM)_h$ model, whilst we consider $(WM1)_h$ and $(WM2)_h$ models for POD-G. As done for the thermal model, we consider four different numerical experiments having different kinds and numbers of parameters:

- *Numerical experiment (i)*: 4 physical parameters: $\Xi = \{k, \mu, \lambda, \alpha\}$.

- *Numerical experiment (ii)*: 4 physical parameters and all 3 geometric parameters: $\Xi = \{k, \mu, \lambda, \alpha, t_0, D_2, D_4\}$.

- *Numerical experiment (iii)*: 4 physical parameters and 6 geometric parameters: $\Xi = \{k, \mu, \lambda, \alpha, t_0, t_2, t_4, D_0, D_2, D_4\}$.

- *Numerical experiment (iv)*: 4 physical parameters and all (10) geometric parameters:
  $\Xi = \{k, \mu, \lambda, \alpha, t_0, t_1, t_2, t_3, t_4, D_0, D_1, D_2, D_3, D_4\}$.

Table 6 shows the total number of samples provided by the full order model, the number of samples used for training and the one used for testing of ANN. For all the numerical experiments, the POD space was computed by considering 1000 snapshots. The eigenvalue plot is shown in Figure 12. Like the thermal model, we observe that the numerical experiment (iv), characterized by the larger number of parameters, shows the lowest decay. On the other hand, as expected, among the different mechanical models we consider, the model $(WM)_h$ exhibits the slowest eigenvalues decay including it both thermal and mechanical effects.

20

(a) Numerical experiment (i).

(b) Numerical experiment (ii).

(c) Numerical experiment (iii).
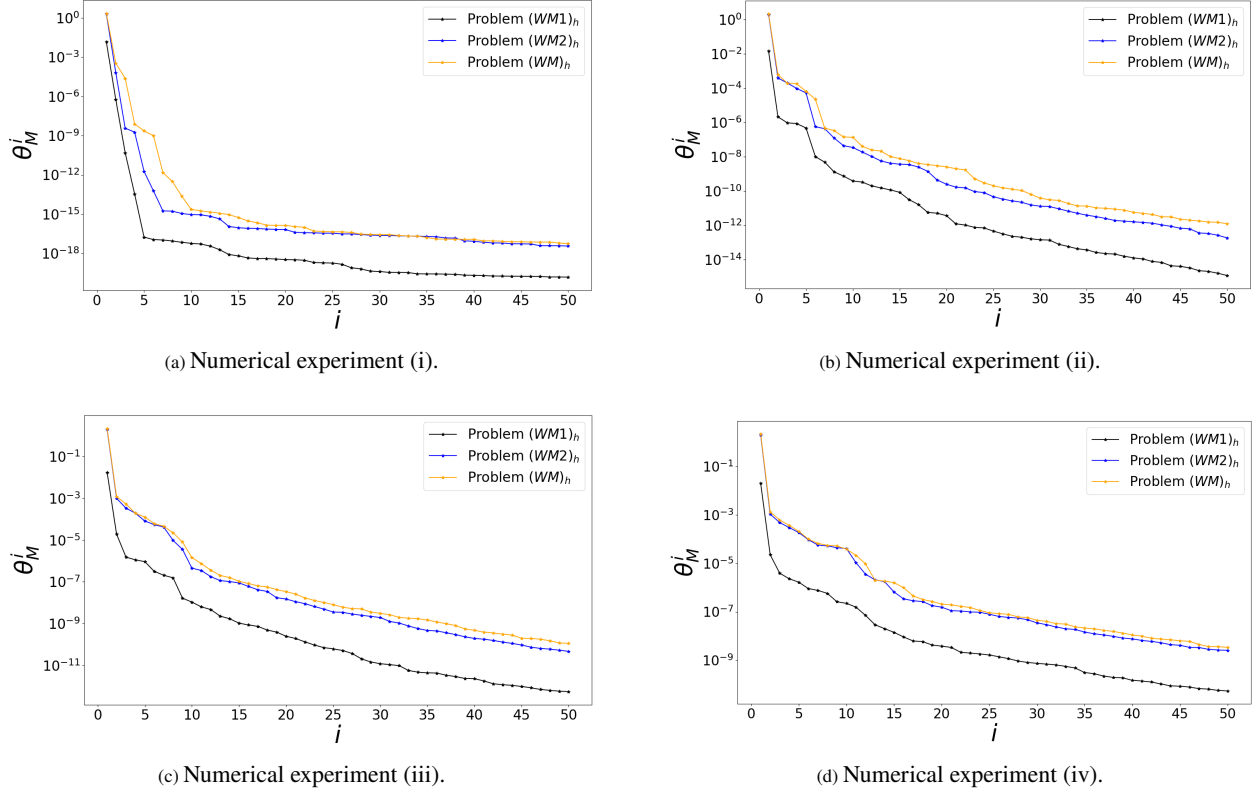

(d) Numerical experiment (iv).

Figure 12: Mechanical model: plot of the eigenvalues $\{\theta_M^i\}_{i=1}^{50}$ sorted in descending order for all the numerical experiments considered.

Figure 13 shows the relative error (69) both for POD-ANN and POD-G. The projection error (70) is also depicted. As observed for the thermal model, POD-G is able to provide more accurate results with respect to POD-ANN.

Figure 14 shows the qualitative comparison between the computed FOM and MOR related to the numerical experiment (iv) for the parameters tuple

$$\Xi = \{2.365, 0.6, 0.6, 0.5, 3.2, 14.10, 8.50, 9.2, 9.9, 10.6, 10, 2.08e9, 1.39e9, 1e-6\} \, .$$

We use 7 POD basis. The POD-ANN solution was computed with $n_{tr} = 2500$ and $H = 130$. We could observe that both MOR approaches are able to provide a good reconstruction of the displacement field. In order to justify our choice to consider separately $(WM1)_h$ and $(WM2)_h$ in the Galerkin projection framework, we also highlight that, as shown in Figure 14, the scale difference between their displacements (derived from mechanical loads for the first and from the thermal ones for the second) is of one order of magnitude. Thus, the use of the model $(WM)_h$ could lead to a less accurate reconstruction of the displacement field.

Finally, we briefly discuss the efficiency of our MOR approach. We report in Table 7 some estimations related to the offline time for all the numerical experiments carried out. We observe that, unlike the thermal model, the time taken by POD is comparable for all the numerical experiments. This is not surprising because in this case we consider the same number of snapshots for the computation of the reduced space for all the numerical experiments. Like the thermal model, the ANN training is faster for the numerical experiment (i), probably because of the minor complexity with respect to the other numerical experiments. Unlike the thermal model, the total offline cost of the POD-ANN method is comparable with the one related the POD-G method. This is because we train two models for the POD-G method that take a similar amount of time as training one model for the POD-ANN method. We report in Table 8 the online time related to the POD-G and POD-ANN methods for all the numerical experiments carried out. Like the thermal model, the online time of POD-G method increases significantly in presence of geometric parameters by moving from $8e-4$ s (numerical experiment (i)) to $2.6/6.9e-2$ s (numerical experiments (ii)-(iv)) for the model $(WM1)_h$ and from $4.5e-2$ s (numerical experiment (i)) to $1.9/2.6e-1$ s (numerical experiments (ii)-(iv)) for the model $(WM2)_h$. We could observe that the online time taken by the model $(WM2)_h$ is significantly greater than that taken by the model $(WM1)_h$. This is expected because for the model $(WM2)_h$ a reduced basis approximation of temperature needs to be computed due to

the thermo-mechanical coupling. On the other hand, the POD-ANN, that does not need reduced basis approximation of temperature thanks to its non intrusive nature, is able to provide a higher computational efficiency. Moreover, like the thermal model, the POD-ANN online time remains relatively constant for all the numerical experiments under investigations, around $5e-4$, by showing a low sensitivity at varying of the kind and number of parameters considered.
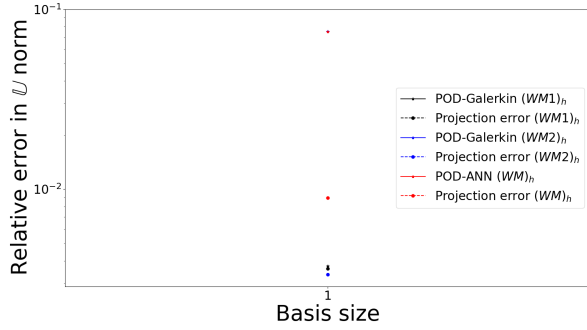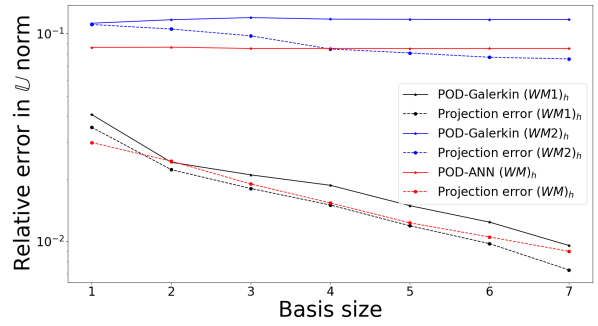

(a) Numerical experiment (i). For POD-ANN $n_{tr} = 500$ and $H = 60$.
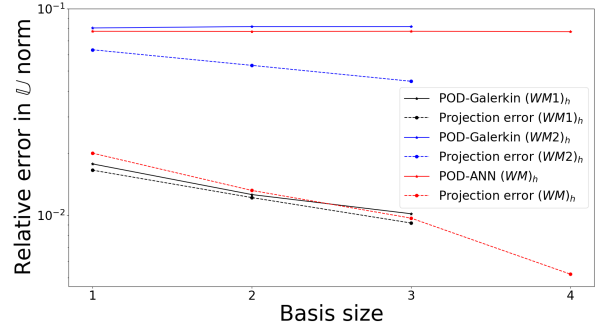
(b) Numerical experiment (ii). For POD-ANN $n_{tr} = 500$ and $H = 80$.
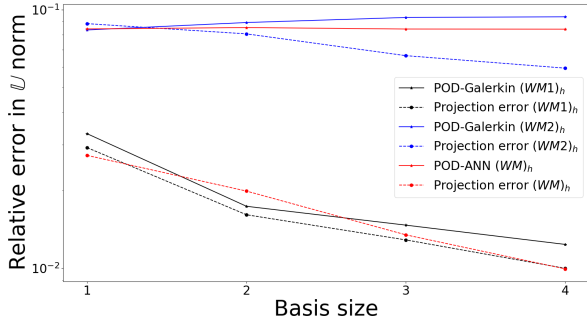
(c) Numerical experiment (iii). For POD-ANN $n_{tr} = 1000$ and $H = 170$.

(d) Numerical experiment (iv). For POD-ANN $n_{tr} = 2500$ and $H = 130$.

Figure 13: Mechanical model: error analysis for POD-G and POD-ANN for all the numerical experiments considered.

	n_{tr}	Training	Testing
Numerical experiment (i)	500	350	150
Numerical experiment (ii)	500	350	150
Numerical experiment (iii)	1000	700	300
Numerical experiment (iv)	2500	1750	750

Table 6: Mechanical model: number of total samples n_{tr} by FOM and number of samples used for training and testing of ANN.

	Basis size	POD-G $(WM1)_h$	POD-G $(WM2)_h$	POD-ANN $(WM)_h$
Numerical experiment (i)	1	8e-4	4.5e-2	6.7e-4
Numerical experiment (ii)	3	2.6e-2	1.9e-1	5.3e-4
Numerical experiment (iii)	4	5.4e-2	2.1e-1	5.2e-4
Numerical experiment (iv)	7	6.9e-2	2.6e-1	4.9e-4

Table 8: Mechanical model: online time (in s) for all the numerical experiments under investigation. Concerning POD-ANN, we use $n_{tr} = 500$, $H = 60$ for the numerical experiment (i), $n_{tr} = 500$, $H = 80$ for the numerical experiment (ii), $n_{tr} = 1000$, $H = 170$ for the numerical experiment (iii) and $n_{tr} = 2500$, $H = 130$ for the numerical experiment (iv).

	t_{off}^{POD-G}		t_{POD}		t_{FOM}	
	$(WM1)_h$	$(WM2)_h$	$(WM1)_h$	$(WM2)_h$	$(WM1)_h$	$(WM2)_h$
Numerical experiment (i)	$\approx 4.2e2$	$\approx 6.2e2$	1.6e1	1.8e1		
Numerical experiment (ii)	$\approx 4.2e2$	$\approx 6.2e2$	1.6e1	1.7e1	4e-1	6e-1
Numerical experiment (iii)	$\approx 4.2e2$	$\approx 6.2e2$	1.8e1	1.7e1		
Numerical experiment (iv)	$\approx 4.2e2$	$\approx 6.2e2$	1.7e1	1.7e1		

(a) Problem $(WM1)_h$ and Problem $(WM2)_h$

	$t_{off}^{POD-ANN}$	t_{POD}	t_{tr}	t_{FOM}	t_{proj}
	$(WM)_h$	$(WM)_h$	$(WM)_h$	$(WM)_h$	$(WM)_h$
Numerical experiment (i)	$\approx 1.1e3$	1.8e1	3.4		8.1e-4
Numerical experiment (ii)	$\approx 1.1e3$	1.8e1	3.7	7e-1	9.2e-4
Numerical experiment (iii)	$\approx 1.5e3$	1.6e1	2.9e1		1.0e-3
Numerical experiment (iv)	$\approx 2.5e3$	1.8e1	7.6e1		9.1e-4

(b) Problem $(WM)_h$

Table 7: Mechanical model: time (in s) taken by (i) the entire offline stage (t_{off}), (ii) the computation of the POD modes (t_{POD}), (iii) the training of ANN (t_{tr}), (iv) the computation of a FOM solution (t_{FOM}) and (v) the projection of a FOM solution on the POD space (t_{proj}). Concerning POD-ANN, we use $n_{tr} = 500$, $H = 60$ for the numerical experiment (i), $n_{tr} = 500$, $H = 80$ for the numerical experiment ii), $n_{tr} = 1000$, $H = 170$ for the numerical experiment (iii) and $n_{tr} = 2500$, $H = 130$ for the numerical experiment (iv).
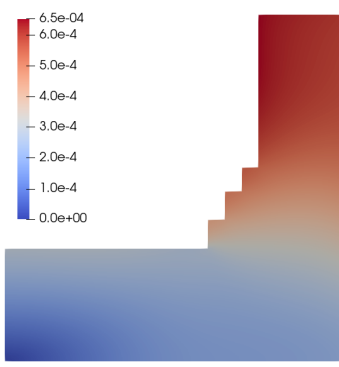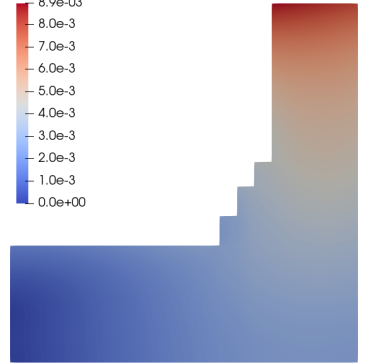

(a) FOM solution related to the problem $(WM1)_h$
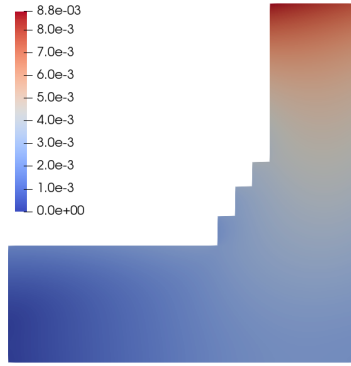
(b) FOM solution related to the problem $(WM2)_h$
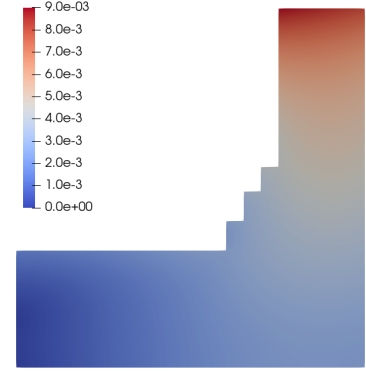
(c) FOM solution related to the problem $(WM)_h$
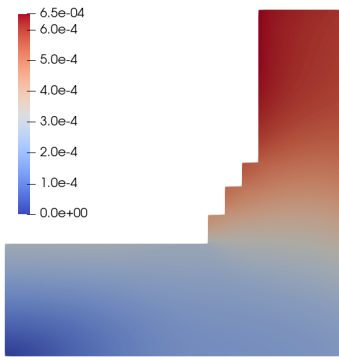
(d) POD-G solution related to the problem $(WM1)_h$
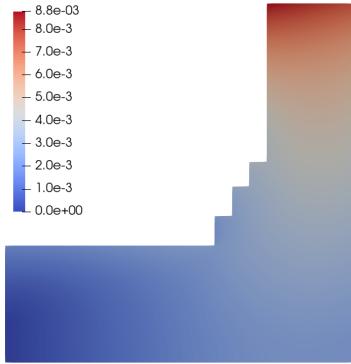
(e) POD-G solution related to the problem $(WM2)_h$

(f) POD-ANN solution related to the problem $(WM)_h$

Figure 14: Mechanical model: comparison between the displacement (in m) computed by FOM and by the POD-G and POD-ANN methods related to the numerical experiment (iv) for $\Xi = \{2.365, 0.6, 0.6, 0.5, 3.2, 14.10, 8.50, 9.2, 9.9, 10.6, 10, 2.08e9, 1.39e9, 1e - 6\}$. We consider 7 POD modes. For POD-ANN, we set $n_{tr} = 2500$ and $H = 130$.

7. Some concluding remarks

In this work we propose a computational pipeline to obtain fast and reliable numerical simulations for one-way coupled steady state linear thermo-mechanical problems in a finite element environment. The test case is referred to a relevant industrial problem related to the investigation of the thermo-mechanical phenomena occurring in blast furnace heart walls. After introducing the main theoretical features of FOM, we detect customized benchmarks for the validation of its numerical implementation. Then we present our MOR framework: we apply POD for the computation of reduced basis space whilst for the evaluation of the modal coefficients we use two different methodologies, the one based on a classic Galerkin projection (POD-G) and the other one based on artificial neural networks (POD-ANN). We found that POD-G is generally more accurate than POD-ANN although POD-ANN exhibits a very higher efficiency, especially when geometric parameters are considered. The higher efficiency of POD-ANN in the case of mechanical model can also be attributed to the fact that the computation of reduced basis approximation of temperature field is not required to compute the reduced basis approximation of the displacement field.

We believe that insights given in this work could help to develop advanced numerical tools in order to deal with complex industrial problems. As a follow-up of this work, we are going to enhance training capacity of the deep learning methods, i.e. to reduce the offline cost, as well as to move towards more complex thermo-mechanical problems involving heterogeneity, orthotropy and non-linearity. Some preliminary efforts, in the latter direction, have been already carried out both at full order [53] and reduced order level [52]. Concerning the POD-Galerkin method, it is expected that the computational efficiency furthermore decreases due to absence of affine expansion for assembling system of equations. Regarding the accuracy of the method, the interpolation of operators could introduce an additional source of error. On the other hand, the POD-ANN method can be properly set to take care of non-linearities by increasing the number of hidden layers and/or their depth. However, the accuracy and the computational efficiency are not likely to change to the significant extent [27, 41].

Appendix A. Validation of the full order model

In this section we verify the numerical implementation of the FOM introduced in Secs. 4 and 5. All the FOM computations have been performed by using the python finite element library FEniCS [1].

We use a mesh of ω containing 121137 triangular elements and 61147 vertices. The minimum mesh size is 0.011 m and the maximum one is 0.045 m. Its minimum quality is $q_e = 0.25$ (eq. 68).

The pipeline that we follow for the design of reliable benchmark tests to be used for the FOM validation consists of three steps:

- We set analytical expressions for temperature and displacement.

- We calculate corresponding model data, including boundary conditions and source terms, in order to identify the FOM for which the analytical relationships are solutions.

- Finally, we numerically solve the problem and compare the computational solutions with the analytical ones.

We consider the physical properties reported in Table A.9 for all numerical simulations shown in this section.

Property	Value
Thermal conductivity k	$10\frac{W}{mK}$
Convection coefficient $h_{c,-}$	$2000\frac{W}{m^2 K}$
Convection coefficient $h_{c,f}$	$200\frac{W}{m^2 K}$
Convection coefficient $h_{c,out}$	$2000\frac{W}{m^2 K}$
Young's modulus E	$5e9Pa$
Poisson's ratio ν	0.2
Thermal expansion coefficient α	$10^{-6}/K$
Reference temperature T_0	$298K$
Gravitational acceleration g	$9.81\frac{m}{s^2}$

Table A.9: Physical properties values used for the FOM benchmark tests.

Appendix A.1. Thermal model

We consider the following analytical expression for the temperature,

$$T_a(r,y) = C'r^2 y, \quad \text{with } C' = 1K/m^3 . \tag{A.1}$$

Then:

- The corresponding source term Q is obtained by using eq. (16),

$$Q(r,y) = -k\frac{\partial^2 T_a}{\partial r^2} - k\frac{\partial^2 T_a}{\partial y^2} - \frac{k}{r}\frac{\partial T_a}{\partial r} = -4C'ky , \tag{A.2}$$

- The heat flux q_+, as well as the temperatures T_f, T_{out} and T_-, are derived from eq. (17),

$$\text{on } \gamma_+ \ : q_+(r,y) = -k\frac{\partial T_a}{\partial y} = -C'kr^2 , \tag{A.3a}$$

$$\text{on } \gamma_{sf} \ : \ T_f = T_a + \frac{k}{h_{c,f}}\left(\frac{\partial T_a}{\partial r}n_r + \frac{\partial T_a}{\partial y}n_y\right)$$

$$= C'r^2 y + C'\frac{k}{h_{c,f}}(2ryn_r + r^2 n_y) , \tag{A.3b}$$

$$\text{on } \gamma_{out} \ : \ T_{out} = T_a + \frac{k}{h_{c,out}}\frac{\partial T_a}{\partial r} = C'r^2 y + C'\frac{2ryk}{h_{c,out}} , \tag{A.3c}$$

$$\text{on } \gamma_- \ : \ T_- = T_a - \frac{k}{h_{c,-}}\frac{\partial T_a}{\partial y} = C'r^2 y - C'\frac{r^2 k}{h_{c,-}} , \tag{A.3d}$$

and it is verified that

$$\text{on } \gamma_s \ : \ \frac{\partial T_a}{\partial r} = 0. \tag{A.4a}$$

We solve the $(WT)_h$ problem for the data $Q, q_+, T_f, T_{out}, T_-$ given by equations (A.2)-(A.4a). We choose a discretized space of polynomial of degree 3. Analytical and numerical solutions are reported in Figure A.15 (left and center). As we can see, a very good agreement is obtained. For a more quantitative comparison, we also display the absolute error in Figure A.15 (right), and compute the relative error,

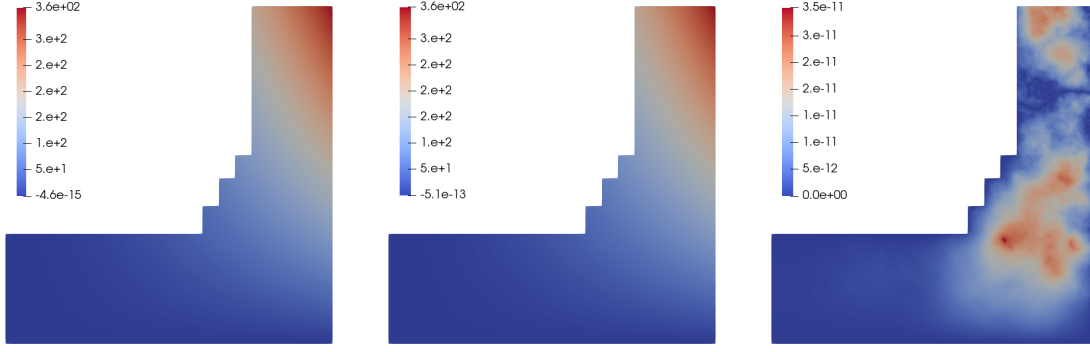$$\frac{||T_a - T_h||_{H_r^1(\omega)}}{||T_a||_{H_r^1(\omega)}} = 7e - 13.$$

25

Figure A.15: Benchmark for the thermal model $(WT)_h$: analytical temperature T_a (left), numerical temperature T_h (center), and corresponding absolute error $|T_a - T_h|$ (right) in K.

Appendix A.2. Mechanical model

Firstly, we consider that the body is at reference temperature $T = T_0$, i.e. thermal stresses $(2\mu + 3\lambda)\alpha(T - T_0)$ are not present. Therefore, we refer to the problem $(WM1)_h$.

We consider a known displacement function

$$\vec{u}_a = C(ry^2, r^2 y), \quad \text{with } C = 1e - 4/m^2. \tag{A.5}$$

Then:

- The components of the stress tensor σ are given by eq. (7) as,

$$\sigma_{rr} = \frac{E}{(1 - 2\nu)(1 + \nu)}(Cy^2 + \nu Cr^2), \tag{A.6a}$$

$$\sigma_{yy} = \frac{E}{(1 - 2\nu)(1 + \nu)}(2\nu Cy^2 + (1 - \nu)Cr^2), \tag{A.6b}$$

$$\sigma_{\theta\theta} = \frac{E}{(1 - 2\nu)(1 + \nu)}(Cy^2 + \nu Cr^2), \tag{A.6c}$$

$$\sigma_{ry} = \frac{2ECry}{(1 + \nu)}. \tag{A.6d}$$

- The source term $\vec{f}_0 = [f_{0,r} \; f_{0,y}]$ is obtained from eqs. (18) and (A.6) as,

$$f_{0,r} = -\left(\frac{\partial \sigma_{rr}}{\partial r} + \frac{\partial \sigma_{ry}}{\partial y} + \frac{\sigma_{rr} - \sigma_{\theta\theta}}{r}\right)$$

$$= -\left(\frac{2E\nu Cr}{(1 - 2\nu)(1 + \nu)} + \frac{2ECr}{(1 + \nu)}\right), \tag{A.7a}$$

$$f_{0,y} = -\left(\frac{\partial \sigma_{ry}}{\partial r} + \frac{\partial \sigma_{yy}}{\partial y} + \frac{\sigma_{ry}}{r}\right)$$

$$= -\left(\frac{4ECy}{(1 + \nu)} + \frac{4E\nu Cy}{(1 - 2\nu)(1 + \nu)}\right). \tag{A.7b}$$

26

- The boundary tractions are derived from eqs. (20) and (A.6) as,

$$\text{on } \gamma_+ : \quad g_{+,r} = \frac{2ECry}{(1+v)} \,, \tag{A.8a}$$

$$g_{+,y} = \frac{E}{(1-2v)(1+v)} \left(2vCy^2 + (1-v)Cr^2 \right) \,, \tag{A.8b}$$

$$\text{on } \gamma_- : \quad g_{-,r} = -\frac{2ECry}{(1+v)} \,, \tag{A.8c}$$

$$\text{on } \gamma_{sf} : \quad g_{sf,r} = \frac{E}{(1-2v)(1+v)} \left(Cy^2 + vCr^2 \right) n_r + \frac{2ECry}{(1+v)} n_y \,, \tag{A.8d}$$

$$g_{sf,y} = \frac{2ECry}{(1+v)} n_r + \frac{E}{(1-2v)(1+v)} \left(2vCy^2 + (1-v)Cr^2 \right) n_y \,, \tag{A.8e}$$

$$\text{on } \gamma_{out} : \quad g_{out,r} = \frac{E}{(1-2v)(1+v)} \left(Cy^2 + vCr^2 \right) \,, \tag{A.8f}$$

$$g_{out,y} = \frac{2ECry}{(1+v)} \,, \tag{A.8g}$$

and it is verified that

$$\text{on } \gamma_- \cup \gamma_s : \quad \overrightarrow{u}_a \cdot \overrightarrow{n} = 0 \,. \tag{A.9a}$$

We solve the $(WM1)_h$ problem for the data given by equations (A.7a) - (A.9a) by using a discretized space of polynomial of degree 3. The magnitude of the analytical and numerical displacement, as well as the associated absolute error, are represented in Figure A.16. Moreover, we compute the relative error

$$\frac{||\overrightarrow{u}_a - \overrightarrow{u}_h||_{\mathbb{U}}}{||\overrightarrow{u}_a||_{\mathbb{U}}} = 1.81e - 12.$$

Like the thermal model, even in this case we could observe that the two solutions show a very good agreement. For further comparison, we also computed the Von Mises stress:

$$\sigma_{vm} = \sqrt{\frac{3}{2} \sigma_d : \sigma_d} \,, \tag{A.10}$$

where σ_d is the deviatoric part of the stress tensor

$$\sigma_d = \sigma - \frac{1}{3} Tr(\sigma) \boldsymbol{I} \,. \tag{A.11}$$

We display the magnitude of the analytical and numerical Von Mises stress, σ_{vma} and σ_{vmh} respectively, and the corresponding absolute error in Figure A.17. We see that a very good matching is obtained.
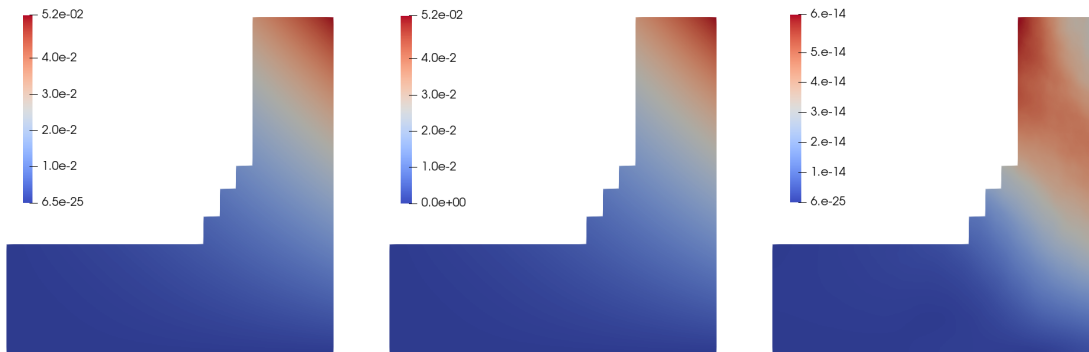

Figure A.16: Benchmark for the mechanical model $(WM1)_h$: analytical displacement magnitude $\lceil \overrightarrow{u}_a \rceil$ (left), numerical displacement magnitude $\lceil \overrightarrow{u}_h \rceil$ (center), and absolute error magnitude $\lceil \overrightarrow{u}_a - \overrightarrow{u}_h \rceil$ (right) in m.
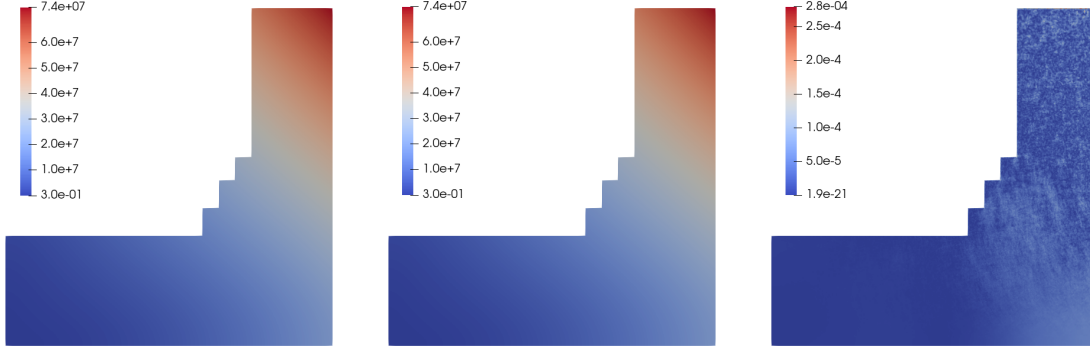
Figure A.17: Benchmark for the mechanical model $(WM1)_h$: analytical Von Mises stress magnitude σ_{vma} (left), numerical Von Mises stress magnitude σ_{vmh} (center), and absolute error $|\sigma_{vmh} - \sigma_{vma}|$ (right) in N/m^2.

Now we address the coupling between the thermal and mechanical effects, so we refer to the problem $(WM)_h$. We assume for the temperature the analytical field used for the problem $(WT)_h$, T_a (see eq. (A.1)), and for the displacement the analytical field used for the problem $(WM1)_h$, $\overrightarrow{u}_a$ (see eq. (A.5)). Then:

- We obtain the thermal stresses from eqs. (3) and (5):

$$(2\mu + 3\lambda)\alpha(T - T_0) = (2\mu + 3\lambda)\alpha(C'r^2y - T_0) = \frac{E}{(1 - 2\nu)}\alpha(C'r^2y - T_0) \ .$$

- The components of the stress tensor σ are given by eqs. (19):

$$\sigma_{rr} = \frac{E}{(1 - 2\nu)(1 + \nu)}(Cy^2 + \nu Cr^2) - \frac{E}{(1 - 2\nu)}\alpha(C'r^2y - T_0) \ , \tag{A.12a}$$

$$\sigma_{yy} = \frac{E}{(1 - 2\nu)(1 + \nu)}(2\nu Cy^2 + (1 - \nu)Cr^2) - \frac{E}{(1 - 2\nu)}\alpha(C'r^2y - T_0) \ , \tag{A.12b}$$

$$\sigma_{\theta\theta} = \frac{E}{(1 - 2\nu)(1 + \nu)}(Cy^2 + \nu Cr^2) - \frac{E}{(1 - 2\nu)}\alpha(C'r^2y - T_0) \ , \tag{A.12c}$$

$$\sigma_{ry} = \frac{2ECry}{(1 + \nu)} \ . \tag{A.12d}$$

- The source term $\overrightarrow{f}_0 = [f_{0,r} \ f_{0,y}]$ is obtained from eqs. (18) and (A.6) by:

$$
\begin{aligned}
f_{0,r} &= -\left(\frac{\partial \sigma_{rr}}{\partial r} + \frac{\partial \sigma_{ry}}{\partial y} + \frac{\sigma_{rr} - \sigma_{\theta\theta}}{r}\right) \\
&= -\left(\frac{2E\nu Cr}{(1 - 2\nu)(1 + \nu)} + \frac{2ECr}{(1 + \nu)} - \frac{2C'ryE\alpha}{(1 - 2\nu)}\right) \ ,
\end{aligned}
\tag{A.13a}
$$

$$
\begin{aligned}
f_{0,y} &= -\left(\frac{\partial \sigma_{ry}}{\partial r} + \frac{\partial \sigma_{yy}}{\partial y} + \frac{\sigma_{ry}}{r}\right) \\
&= -\left(\frac{4ECy}{(1 + \nu)} + \frac{4E\nu Cy}{(1 - 2\nu)(1 + \nu)} - \frac{C'r^2E\alpha}{(1 - 2\nu)}\right) \ .
\end{aligned}
\tag{A.13b}
$$

28

- The boundary tractions are derived from eqs. (20) and (A.6) as:

$$\text{on } \gamma_+ \ : \ g_{+,r} = \frac{2ECry}{(1+\nu)} \,, \tag{A.14a}$$

$$g_{+,y} = \frac{E}{(1-2\nu)(1+\nu)} \left(2\nu Cy^2 + (1-\nu)Cr^2 \right)$$

$$- \frac{E\alpha}{(1-2\nu)}(C'r^2 y - T_0) \,, \tag{A.14b}$$

$$\text{on } \gamma_- \ : \ g_{-,r} = -\frac{2ECry}{(1+\nu)} \,, \tag{A.14c}$$

$$\text{on } \gamma_{sf} \ : \ g_{sf,r} = \frac{E}{(1-2\nu)(1+\nu)}(Cy^2 + \nu Cr^2)n_r$$

$$- \frac{E\alpha}{(1-2\nu)}(C'r^2 y - T_0)n_r + \frac{2ECry}{(1+\nu)}n_y \,, \tag{A.14d}$$

$$g_{sf,y} = \frac{E}{(1-2\nu)(1+\nu)} \left(2\nu Cy^2 + (1-\nu)Cr^2 \right) n_y$$

$$- \frac{E\alpha}{(1-2\nu)}(C'r^2 y - T_0)n_y + \frac{2ECry}{(1+\nu)}n_r \,, \tag{A.14e}$$

$$\text{on } \gamma_{out} \ : \ g_{out,r} = \frac{E}{(1-2\nu)(1+\nu)}(Cy^2 + \nu Cr^2) - \frac{E\alpha}{(1-2\nu)}(C'r^2 y - T_0) \,, \tag{A.14f}$$

$$g_{out,y} = \frac{2ECry}{(1+\nu)} \,. \tag{A.14g}$$

We display the magnitude of the analytical displacement and Von Mises stress comparing them with the corresponding numerical values in Figures A.18 and A.19, respectively, and compute the relative error

$$\frac{||\vec{u}_a - \vec{u}_h||_{\mathbb{U}}}{||\vec{u}_a||_{\mathbb{U}}} = 2.2e - 12.$$

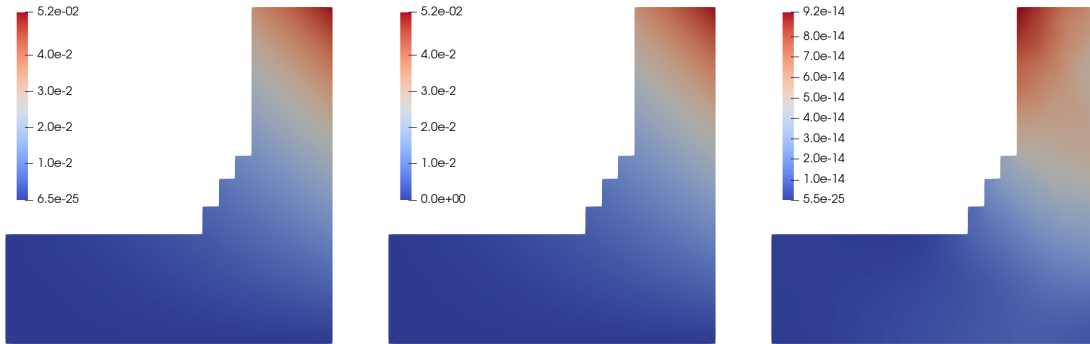We could see that, as for mechanical model $(WM1)_h$, the agreement between the two solutions is very good.

Figure A.18: Benchmark for the mechanical problem $(WM)_h$: analytical displacement magnitude $\lceil \vec{u}_a \rceil$ (left), numerical displacement magnitude $\lceil \vec{u}_h \rceil$ (center), and absolute error $\lceil \vec{u}_a - \vec{u}_h \rceil$(right) in m.
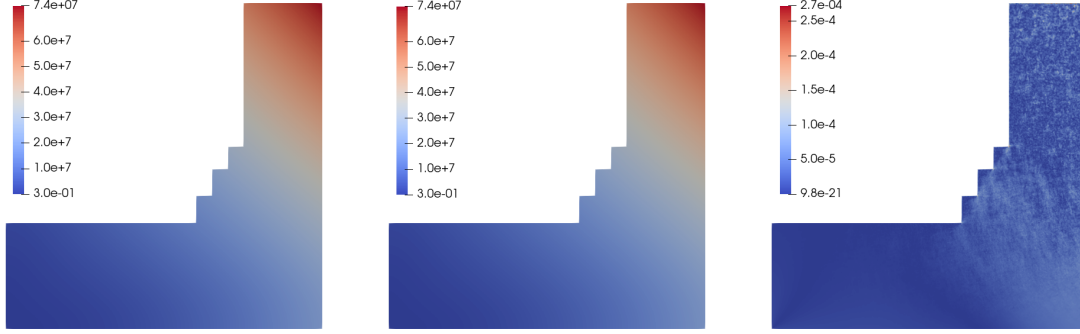
Figure A.19: Benchmark for the mechanical problem $(WM)_h$: analytical Von Mises stress σ_{vma} (left), numerical Von Mises stress σ_{vmh} (center) and absolute error $|\sigma_{vmh} - \sigma_{vma}|$ (right) in N/m^2.
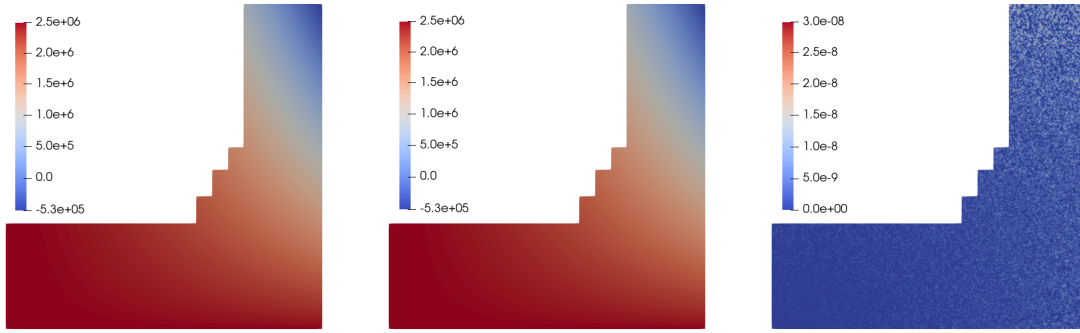

Figure A.20: Benchmark for the mechanical model $(WM2)_h$: difference between the hydrostatic stress computed with the $(WM)_h$ model and the $(WM1)_h$ model $\frac{1}{3} tr \left(\sigma(\overrightarrow{u_h})[T_h] - \sigma(\overrightarrow{u_h})[T_0] \right)$ (left), thermal stress $(2\mu + 3\lambda)\alpha(T_h - T_0)$ (center) and corresponding absolute error $\left| \frac{1}{3} tr \left(\sigma(\overrightarrow{u_h})[T_h] - \sigma(\overrightarrow{u_h})[T_0] \right) - (2\mu + 3\lambda)\alpha(T_h - T_0) \right|$ (right) in N/m^2.

Finally, we observe that the difference between the hydrostatic stress computed with the model $(WM)_h$ and the one computed with the model $(WM1)_h$, i.e. the hydrostatic stress related to the model $(WM2)_h$, should be equal to the thermal stress:

$$\frac{1}{3} tr \left(\boldsymbol{\sigma}(\overrightarrow{u_h})[T_h] - \boldsymbol{\sigma}(\overrightarrow{u_h})[T_0] \right) = (2\mu + 3\lambda)\alpha(T_h - T_0)\boldsymbol{I}. \tag{A.15}$$

The right and hand sides of eq. (A.15) are shown in Figure A.20. We obtain a very good agreement.

References

[1] Alnæs, M.S., Blechta, J., Hake, J., Johansson, A., Kehlet, B., Logg, A., Richardson, C., Ring, J., Rognes, M.E., Wells, G.N., 2015. The fenics project version 1.5. Archive of Numerical Software 3.

[2] Amsallem, D., Cortial, J., Carlberg, K., Farhat, C., 2009. A method for interpolating on manifolds structural dynamics reduced-order models. International Journal for Numerical Methods in Engineering 80, 1241–1258.

[3] Bader, E., Kärcher, M., Grepl, M., Veroy, K., 2016. Certified reduced basis methods for parametrized distributed elliptic optimal control problems with control constraints. SIAM Journal on Scientific Computing 38, A3921–A3946.

[4] Balla, K., Sevilla, R., Hassan, O., Morgan, K., 2021. An application of neural networks to the prediction of aerodynamic coefficients of aerofoils and wings. Applied Mathematical Modelling 96, 456–479.

[5] Barral, P., Pérez-Pérez, L., Quintela, P., 2022a. Numerical simulation of the transient heat transfer in a blast furnace main trough during its complete campaign cycle. International Journal of Thermal Sciences 173, 107349.

[6] Barral, P., Pérez-Pérez, L., Quintela, P., 2022b. Transient thermal response with nonlocal radiation of a blast furnace main trough. Applied Mathematical Modelling 105, 197–225.

[7] Barrault, M., Maday, Y., Nguyen, N.C., Patera, A.T., 2004. An 'empirical interpolation' method: application to efficient reduced-basis discretization of partial differential equations. Comptes Rendus Mathematique 339, 667–672.

[8] Benner, P., Gugercin, S., Willcox, K., 2015a. A survey of projection-based model reduction methods for parametric dynamical systems. SIAM Review 57, 483–531.

[9] Benner, P., Herzog, R., Lang, N., Riedel, I., Saak, J., 2019. Comparison of model order reduction methods for optimal sensor placement for thermo-elastic models. Engineering Optimization 51, 465–483.

[10] Benner, P., Ohlberger, M., Patera, A., Rozza, G., Urban, K., 2015b. A survey of projection-based model reduction methods for parametric dynamical systems. SIAM Review 57, 483–531.

[11] Benner, P., Schilders, W., Grivet-Talocia, S., Quarteroni, A., Rozza, G., Silveira, L.M. (Eds.), 2020. Model Order Reduction. De Gruyter.

[12] Bermúdez de Castro, A., 2005. Continuum thermomechanics. Progress in Mathematical Physics 43.

[13] Brezis, H., 2010. Functional Analysis, Sobolev Spaces and Partial Differential Equations. Universitext, Springer New York.

[14] Brulin, J., Rekik, A., Blond, E., Josserand, L., Gasser, A., Roulet, F., 2011. Thermomechanical modelling of a blast furnace hearth, UNITECR'11, Kyoto, Japan. pp. CD–ROM. hal-00651546.

[15] Cameron, I., Sukhram, M., Lefebvre, K., Davenport, W., 2019. Blast furnace ironmaking : Analysis, control, and optimization, Elsevier.

[16] Chen, W., Wang, Q., Hesthaven, J.S., Zhang, C., 2021. Physics-informed machine learning for reduced-order modeling of nonlinear problems. Journal of Computational Physics 446, 110666.

[17] Demo, N., Strazzullo, M., Rozza, G., 2021. An extended physics informed neural network for preliminary analysis of parametric optimal control problems. `arXiv:2110.13530`.

[18] Demo, N., Tezzele, M., Rozza, G., 2019. A non-intrusive approach for the reconstruction of pod modal coefficients through active subspaces. Comptes Rendus Mécanique 347, 873–881. Data-Based Engineering Science and Technology.

[19] FEniCS, URL: `www.fenicsproject.org`. Accessed: 04-December-2021.

[20] Geerdes, M., Chaigneau, R., Lingiardi, O., 2020. Modern Blast Furnace Ironmaking: An Introduction (Fourth Edition, 2020). IOS Press.

[21] Gurtin, M., 1981. An Introduction to Continuum Mechanics. Academic Press.

[22] Gurtin, M.E., Fried, E., Anand, L., 2010. The Mechanics and Thermodynamics of Continua. Cambridge University Press.

[23] Guérin, N., Thorin, A., Thouverez, F., Legrand, M., Almeida, P., 2018. Thermomechanical Model Reduction for Efficient Simulations of Rotor-Stator Contact Interaction. Journal of Engineering for Gas Turbines and Power 141.

[24] Haasdonk, B., 2017. Reduced Basis Methods for Parametrized PDEs—A Tutorial Introduction for Stationary and Instationary Problems. chapter 2. pp. 65–136.

[25] Haykin, S., 2009. Neural Networks and Learning Machines. Number v. 10 in Neural networks and learning machines, Prentice Hall.

[26] Hernández-Becerro, P., Spescha, D., Wegener, K., 2021. Model order reduction of thermo-mechanical models with parametric convective boundary conditions: focus on machine tools. Computational Mechanics 67, 167–184.

[27] Hesthaven, J., Ubbiali, S., 2018. Non-intrusive reduced order modeling of nonlinear problems using neural networks. Journal of Computational Physics 363, 55 – 78.

[28] Hesthaven, J.S., Rozza, G., Stamm, B., 2015. Certified Reduced Basis Methods for Parametrized Partial Differential Equations. SpringerBriefs in Mathematics, Springer International Publishing.

[29] Hlaváček, I., 1989. Korn's inequality uniform with respect to a class of axisymmetric bodies. Aplikace Matematiky 34, 146–154.

[30] Hlaváček, I., 1989. Shape optimization of elastic axisymmetric bodies. Aplikace matematiky 34, 225–245.

[31] Hoang, K.C., Kim, T.Y., 2017. Fast and accurate two-field reduced basis approximation for parametrized thermoelasticity problems. Finite Elements in Analysis and Design 141, 96–118.

[32] Huynh, D., Patera, A., 2007. Reduced basis approximation and a posteriori error estimation for stress intensity factors. International Journal for Numerical Methods in Engineering 72, 1219–1259.

[33] Iman, R.L., 2008. Latin Hypercube Sampling. John Wiley & Sons, Ltd.

[34] Kingma, D.P., Ba, J., 2015. Adam: A method for stochastic optimization, 3rd International Conference on Learning Representations (ICLR). `arXiv:1412.6980`.

[35] Li, H., 2011. Finite element analysis for the axisymmetric laplace operator on polygonal domains. J. Computational Applied Mathematics 235, 5155–5176.

[36] Li, Z., Kovachki, N., Azizzadenesheli, K., Liu, B., Bhattacharya, K., Stuart, A., Anandkumar, A., 2020. Neural operator: Graph kernel network for partial differential equations. `arXiv:2003.03485`.

[37] Li, Z., Kovachki, N., Azizzadenesheli, K., Liu, B., Bhattacharya, K., Stuart, A., Anandkumar, A., 2021. Fourier neural operator for parametric partial differential equations. `arXiv:2010.08895`.

[38] Meneghetti, L., Demo, N., Rozza, G., 2021. A dimensionality reduction approach for convolutional neural networks. `arXiv:2110.09163`.

[39] Necas, J., 1967. Les Methodes Directes en Theorie Des Equations Elliptiques Jindrich Necas. Masson.

[40] Paszke, A., Gross, S., Massa, F., Lerer, A., Bradbury, J., Chanan, G., Killeen, T., Lin, Z., Gimelshein, N., Antiga, L., Desmaison, A., Kopf, A., Yang, E., DeVito, Z., Raison, M., Tejani, A., Chilamkurthy, S., Steiner, B., Fang, L., Bai, J., Chintala, S., 2019. Pytorch: An imperative style, high-performance deep learning library, in: Wallach, H., Larochelle, H., Beygelzimer, A., d'Alché-Buc, F., Fox, E., Garnett, R. (Eds.), Advances in Neural Information Processing Systems 32. Curran Associates, Inc., pp. 8024–8035.

[41] Pichi, F., Ballarin, F., Rozza, G., Hesthaven, J.S., 2021. An artificial neural network approach to bifurcating phenomena in computational fluid dynamics. `arXiv:2109.10765`.

[42] PyTorch, URL: `www.pytorch.org`. Accessed: 04-December-2021.

[43] Quarteroni, A., Manzoni, A., Negri, F., 2016. Reduced Basis Methods for Partial Differential Equations. Number v. 1 in La Matematica per il 3+2, Springer International Publishing.

[44] Raissi, M., Perdikaris, P., Karniadakis, G., 2019. Physics-informed neural networks: A deep learning framework for solving forward and inverse problems involving nonlinear partial differential equations. Journal of Computational Physics 378, 686–707.

[45] Raissi, M., Yazdani, A., Karniadakis, G.E., 2020. Hidden fluid mechanics: Learning velocity and pressure fields from flow visualizations. Science 367, 1026–1030.

[46] RBniCS, URL: `www.rbnicsproject.org`. Accessed: 04-December-2021.

[47] Rojas, R., 1996. Neural Networks: A Systematic Introduction. Springer-Verlag, Berlin, Heidelberg.

[48] Rozza, G., Huynh, D., Patera, A., 2007. Reduced basis approximation and a posteriori error estimation for affinely parametrized elliptic coercive partial differential equations. Archives of Computational Methods in Engineering 15.

[49] San, O., Maulik, R., Ahmed, M., 2019. An artificial neural network framework for reduced order modeling of transient flows. Communications in Nonlinear Science and Numerical Simulation 77, 271–287.

[50] Schilders, W., 2008. Introduction to Model Order Reduction. Springer Berlin Heidelberg, Berlin, Heidelberg. pp. 3–32.

[51] Schilders, W.H.A., Lutowska, A., 2014. A Novel Approach to Model Order Reduction for Coupled Multiphysics Problems. Springer International Publishing, Cham. pp. 1–49.

[52] Shah, N.V., Girfoglio, M., Barral, P., Rozza, G., Quintela, P., Lengomin, A., 2022. Coupled parameterized reduced order modelling of thermomechanical phenomena arising in blast furnaces. Ph.D. thesis. Scuola Internazionale Superiore di Studi Avanzati. URL: hdl.handle.net/20.500.11767/127929.

[53] Shah, N.V., Girfoglio, M., Rozza, G., 2021. Thermomechanical modelling for industrial applications. arXiv:2108.13366.

[54] Sinha, T., Sikka, K., Lall, R., 2021. Artificial neural networks and bayesian techniques for flip-chip package thermo-mechanical analysis, 2021 IEEE 71st Electronic Components and Technology Conference (ECTC), pp. 1442–1449.

[55] Swartling, M., Sundelin, B., Tilliander, A., Jönsson, P.G., 2010. Heat transfer modelling of a blast furnace hearth. steel research international 81, 186–196.

[56] Vizzaccaro, A., Givois, A., Longobardi, P., Shen, Y., Deü, J.F., Salles, L., Touzé, C., Thomas, O., 2020. Non-intrusive reduced order modelling for the dynamics of geometrically nonlinear flat structures using three-dimensional finite elements. Computational Mechanics 66, 1293–1319.

[57] Vázquez-Fernández, S., García-Lengomín Pieiga, A., Lausín-Gónzalez, C., Quintela, P., 2019. Mathematical modelling and numerical simulation of the heat transfer in a trough of a blast furnace. International Journal of Thermal Sciences 137, 365 – 374.

[58] Wang, Q., Hesthaven, J.S., Ray, D., 2019. Non-intrusive reduced order modeling of unsteady flows using artificial neural networks with application to a combustion problem. Journal of Computational Physics 384, 289–307.

[59] Zhang, G., Eddy Patuwo, B., Y. Hu, M., 1998. Forecasting with artificial neural networks:: The state of the art. International Journal of Forecasting 14, 35–62.

[60] Zhang, S., Oskay, C., 2017. Reduced order variational multiscale enrichment method for thermo-mechanical problems. Computational Mechanics 59, 887–907.

[61] Zienkiewicz, O.C., Taylor, R.L., Zhu, J.Z., 2005. The Finite Element Method: Its Basis and Fundamentals. 6 ed., Butterworth-Heinemann.